

## USING REDUCED MESHES FOR SIMULATIONS OF THE LOCALIZATION OF SMALL ELECTROMAGNETIC INHOMOGENEITIES IN A 3D BOUNDED DOMAIN

M. ASCH AND S.M. MEFIRE

(Communicated by Gang Bao)

**Abstract.** We are concerned in this work with simulations of the localization of a finite number of small electromagnetic inhomogeneities contained in a three-dimensional bounded domain. Typically, the underlying inverse problem considers the time-harmonic Maxwell equations formulated in electric field in this domain and attempts, from a finite number of boundary measurements, to localize these inhomogeneities. Our simulations are based on an approach that combines an asymptotic formula for perturbations in the electromagnetic fields, a suited inversion process, and finite element meshes derived from a non-standard discretization process of the domain. As opposed to a recent work, where the usual discretization process of the domain was employed in the computations, here we localize inhomogeneities that are one order of magnitude smaller.

**Key words.** inverse problems, Maxwell equations, electric fields, inhomogeneities, Current Projection method, MUSIC method, FFT, edge elements, numerical measurements, composite numerical integrations.

### 1. Introduction

This work falls directly in the field of Electrical Impedance Tomography. We seek to recover unknown inhomogeneities contained in a bounded domain from a finite number of measurements evaluated on its boundary. From a practical point of view, such measurements are experimental (or physical) whereas from a simulation point of view, they are numerically evaluated. Usually in this simulation context, we solve the underlying inverse problem with the help of a localization procedure that considers, as data, numerical boundary measurements. Typically, each one of these measurements results from a numerical computation of the physical field present in the domain, due to a current applied on its boundary.

In simulations of the localization of small electromagnetic inhomogeneities contained in a three-dimensional bounded domain, we must for instance compute by a finite element method the electric (or magnetic) field, induced by each prescribed boundary current, in order to evaluate numerically the corresponding boundary measurement of “voltage” type. When the required finite element method is based on the usual triangulation process of the domain, we are concerned, for each prescribed boundary current, with a discrete formulation in electric (or magnetic) field which is numerically expensive to solve. In fact, the usual triangulation process generates a “full” conforming mesh of the domain that implicitly takes into account the discretization of each inhomogeneity and leads to a very large number of degrees of freedom caused by the smallness of the inhomogeneities — especially as this is a three-dimensional domain and as mixed finite elements are considered. The discrete system deriving from the afore-mentioned formulation then has a very

---

Received by the editors July 18, 2007 and, in revised form, January 16, 2008.

2000 *Mathematics Subject Classification.* 65N21, 65N30, 78A25.

This work was partly supported by ACI NIM (171) from the French Ministry of Education and Scientific Research.

large number of unknowns and even by solving this system with preconditioning techniques, we observe, as in [6], that the CPU time needed to evaluate numerically each boundary measurement remains important. In the presence of a large number of small inhomogeneities, the number of degrees of freedom associated with the discrete formulation is excessive and can forbid numerical simulations due now to the exorbitant requirements in memory storage. Considering then a full conforming mesh of the domain when it contains multiple small inhomogeneities leads to some drastic drawbacks regarding the numerical localization as far as memory storage and CPU time are concerned.

Here we are interested in simulations of the localization of small electromagnetic inhomogeneities in a three-dimensional bounded domain, based on finite element meshes that derive from a non-standard discretization process of the domain. This process is aimed at overcoming the drawbacks inherent in full meshes.

As opposed to [6], where full meshes were considered for the localization of inhomogeneities and where we were limited in simulations by the smallness of the inhomogeneities, we expect here to be able to perform localization of much smaller inhomogeneities.

Our approach will also be based on the framework recently proposed by H. Amari, M.S. Vogelius & D. Volkov [4]. Typically, this framework considers the time-harmonic Maxwell equations in a three-dimensional bounded domain  $\Omega$  containing a finite number  $m$  of unknown inhomogeneities of small volume, and proposes to localize these inhomogeneities from an asymptotic expansion of the perturbation in the (tangential) boundary magnetic field. In the presence of well-separated inhomogeneities, and also distant from  $\partial\Omega$ , the boundary of  $\Omega$ , the asymptotic expansion states that, for any  $z \in \partial\Omega$ ,

$$\begin{aligned}
 (1) \quad & (H_\alpha - H_0)(z) \times \nu(z) - 2 \int_{\partial\Omega} \text{curl}_z(\Phi^k(x, z)(H_\alpha - H_0)(x) \times \nu(x)) \times \nu(z) d\sigma_x \\
 & = 2\alpha^3 \omega^2 \sum_{j=1}^m \frac{\mu_0}{\mu_j} (\mu_0 - \mu_j) G(z_j, z) \times \nu(z) M^j \left( \frac{\mu_0}{\mu_j} \right) H_0(z_j) \\
 & + 2\alpha^3 \sum_{j=1}^m \left( \frac{1}{\varepsilon_j} - \frac{1}{\varepsilon_0} \right) ((\text{curl}_x G)(z_j, z))^T \times \nu(z) M^j \left( \frac{\varepsilon_0}{\varepsilon_j} \right) (\text{curl}_x H_0)(z_j) + O(\alpha^4).
 \end{aligned}$$

In (1),  $\alpha$  is the common order of magnitude of the diameters of the inhomogeneities, and the points  $z_j$ ,  $1 \leq j \leq m$ , represent the 'centers' of the inhomogeneities. The magnetic field is denoted by  $H_\alpha$  in the presence of the inhomogeneities and by  $H_0$  in the absence of inhomogeneities. The outward unit normal to  $\Omega$  is represented by  $\nu$ , and  $\omega$  is a given frequency. The (constant) background magnetic permeability and complex permittivity are  $\mu_0$  and  $\varepsilon_0$  respectively. Also,  $\mu_j$  and  $\varepsilon_j$  are the (constant) magnetic permeability and the complex permittivity of the  $j$ th inhomogeneity,  $k^2 = \omega^2 \varepsilon_0 \mu_0$ ,  $\Phi^k$  is the "free space" Green's function for the Helmholtz operator  $\Delta + k^2$ . The operators applied to the matrix valued function  $G$  act column-by-column, and  $G(x, z)$  is the "free space" Green's function for the "background" magnetic problem:  $\text{curl}_x \left( \frac{1}{\varepsilon_0} \text{curl}_x G(x, z) \right) - \omega^2 \mu_0 G(x, z) = -\delta_z I_3$ , with  $I_3$  the  $3 \times 3$  identity matrix,  $\delta_z$  the Dirac delta at  $z$ . Also in (1), the superscript "T" denotes the transpose,  $M^j \left( \frac{\mu_0}{\mu_j} \right)$  and  $M^j \left( \frac{\varepsilon_0}{\varepsilon_j} \right)$  are the polarization tensors associated with the  $j$ th inhomogeneity (symmetric  $3 \times 3$  matrices). Finally, the notation  $O(\alpha^4)$

means a term that goes to zero like  $\alpha^4$ , uniformly in  $z$ .

We will consider an analogous asymptotic expansion to (1), devoted to the study of perturbations in the tangential boundary trace of the curl of the *electric field* due to the presence of inhomogeneities in  $\Omega$ . Then a reformulation will lead to an asymptotic formula that will allow us to evaluate boundary measurements of “voltage” type from prescribed boundary currents. This framework is well adapted to the kinds of applications where it is not necessary to reconstruct the precise values of the electromagnetic parameters of the inhomogeneities or their shapes, but where we are primarily interested in their positions in  $\Omega$ . Our localization approach will mainly consist of locating the ‘centers’ of the inhomogeneities and in some situations, when  $m = 1$ , of estimating moreover the diameter of the inhomogeneity, all this at a fixed frequency  $\omega$ . For other numerical methods aimed at solving the reconstruction problem of inhomogeneities in different settings (conductivity context, dielectric context, ...), we refer to [3], [7], [9], [11], [15], [17], [20], [21], [22].

This work is subdivided into six sections. In Section 2, we introduce, with the help of the time-harmonic Maxwell equations, the weak formulation in electric field in the presence of inhomogeneities in  $\Omega$ . In Section 3, we consider the asymptotic formula for generating boundary measurements of “voltage” type. We start by describing in Section 4 a non-standard discretization process of  $\Omega$  aimed at generating meshes, called the *reduced meshes*, allowing us to overcome the drawbacks inherent in the use of full finite element meshes. Typically, a reduced mesh represents a conforming mesh of  $\Omega$  whose size is bigger than the largest of the diameters of the inhomogeneities present in  $\Omega$ , and which is (explicitly) combined with integration meshes for taking into account the characteristics of these inhomogeneities. Namely, a reduced mesh is (uniquely) made up of tetrahedra of two types: the *inhomogeneous tetrahedra* and the others. An inhomogeneous tetrahedron corresponds to a tetrahedron which surrounds a single inhomogeneity, and with which an integration mesh is explicitly associated. Since we are concerned with inhomogeneities of very small diameters, the size of a reduced mesh of  $\Omega$  can be taken as small as the size of a “fine” mesh of  $\Omega$  that could be considered in the absence of the inhomogeneities. By using a reduced mesh of  $\Omega$  in association with edge elements, we also describe in this section the discrete formulation that allows us to compute the electric field from each prescribed boundary current for evaluating numerically the corresponding boundary measurement. Section 5 presents numerical results obtained from extensive simulations by distinctly considering three localization procedures: the procedure based on the Current Projection method, the procedure deriving from the MUSIC (Multiple Signal Classification) approach, and the one based on an Inverse Fourier method. Each one of these procedures, defined in association with the asymptotic formula that allows us to generate boundary measurements, was already presented in the numerical localization context considering full finite element meshes [6]. Using then reduced meshes here, we first describe numerical results that derive from the procedure based on the Current Projection method, namely in the single inhomogeneity configuration. We next present results obtained from the procedures based on the MUSIC approach and on an Inverse Fourier method, both in the configuration of a single inhomogeneity and in that of multiple inhomogeneities. Finally, we report in Section 6 some conclusions and perspectives.

## 2. Some Notation and the Formulation in Electric Field

Let  $\Omega$  be a bounded open subset of  $\mathbb{R}^3$ , with a smooth boundary  $\partial\Omega$ . For simplicity we take  $\partial\Omega$  to be  $C^\infty$ , but this regularity condition could be considerably weakened. The domain  $\Omega$  contains here a finite number  $m$  of inhomogeneities, each one of the form  $z_j + \alpha B_j$ , where  $B_j \subset \mathbb{R}^3$  is a bounded, smooth ( $C^\infty$ ) domain containing the origin. The total collection of inhomogeneities thus takes the form  $I_\alpha = \bigcup_{j=1}^m (z_j + \alpha B_j)$ . The points  $z_j \in \Omega$ ,  $1 \leq j \leq m$ , that determine the locations of the inhomogeneities are assumed to satisfy:

$$(2) \quad \begin{cases} d_0 \leq |z_j - z_k| & \forall j \neq k, \\ d_0 \leq \text{dist}(z_j, \partial\Omega) & \forall j, \end{cases}$$

where  $d_0 \in \mathbb{R}_+^*$  is fixed. The parameter  $\alpha > 0$ , the common order of magnitude of the diameters of the inhomogeneities, is sufficiently small in such a way that these inhomogeneities are disjoint and their distance to  $\mathbb{R}^3 \setminus \Omega$  is larger than  $d_0/2$ . As a consequence of the assumption (2), it follows that:  $m \leq 6|\Omega|/\pi d_0^3$ . Hereafter, we call each one of these small inhomogeneities, an *imperfection*.

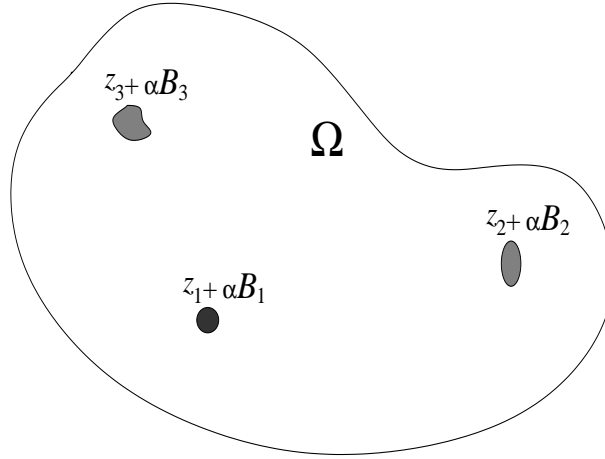


FIGURE 1. An example of a domain containing imperfections.

When we study the time-harmonic solutions of linear Maxwell equations in the domain  $\Omega$  containing different materials, we consider  $\mathbb{C}^3$ -valued fields  $E$ ,  $H$  such that:  $\forall x \in \Omega$ ,

$$(3) \quad \text{curl } E(x) = i\omega\mu(x)H(x), \quad \text{curl } H(x) = -i\omega\varepsilon(x)E(x),$$

where  $\omega > 0$  denotes the given frequency,  $\mu$  is the magnetic permeability,  $\varepsilon(x) = \varepsilon^{\text{re}}(x) + i\frac{\sigma(x)}{\omega}$  represents the complex permittivity, with  $\varepsilon^{\text{re}}$  the (real) electric permittivity and  $\sigma$  the conductivity of the medium. By dividing the first equation of (3) by  $\mu$  and taking the curl, we obtain the following equation for  $E$ :

$$(4) \quad \text{curl}\left(\frac{1}{\mu} \text{curl } E\right) - \omega^2\varepsilon E = 0 \quad \text{in } \Omega.$$

The outward unit normal to  $\Omega$ , defined on  $\partial\Omega$ , will be denoted by  $\nu$ . We shall prescribe non-trivial boundary conditions for  $E \times \nu$ , on  $\partial\Omega$ , in order to arrive at particular non-trivial solutions to (4).

Let  $\mu_0 > 0$ ,  $\varepsilon_0^{\text{re}} > 0$ , and  $\sigma_0 \geq 0$  denote the permeability, the (real) permittivity, and the conductivity of the background medium, with  $\varepsilon_0 = \varepsilon_0^{\text{re}} + i\frac{\sigma_0}{\omega}$  the background complex permittivity. Let also  $\mu_j > 0$ ,  $\varepsilon_j^{\text{re}} > 0$ ,  $\sigma_j \geq 0$  and  $\varepsilon_j = \varepsilon_j^{\text{re}} + i\frac{\sigma_j}{\omega}$  denote the permeability, the (real) permittivity, the conductivity, and the complex permittivity of the  $j$ th imperfection  $z_j + \alpha B_j$ . For simplicity, we shall assume here that all these parameters are constants. Introduce thus the piecewise constant magnetic permeability  $\mu_\alpha$  and the piecewise constant complex permittivity  $\varepsilon_\alpha$ :  $\forall x \in \Omega$ ,

$$\mu_\alpha(x) = \begin{cases} \mu_0, & \text{if } x \in \Omega \setminus \overline{I_\alpha}, \\ \mu_j, & \text{if } x \in z_j + \alpha B_j, \end{cases} \quad \varepsilon_\alpha(x) = \begin{cases} \varepsilon_0, & \text{if } x \in \Omega \setminus \overline{I_\alpha}, \\ \varepsilon_j, & \text{if } x \in z_j + \alpha B_j, \end{cases}$$

with  $1 \leq j \leq m$ . If we allow the degenerate case  $\alpha = 0$ , then the function  $\mu_\alpha$  equals the constant  $\mu_0$  and the function  $\varepsilon_\alpha$  equals the constant  $\varepsilon_0$ .

The electric field denoted  $E_\alpha$ , in the presence of imperfections, satisfies:

$$(5) \quad \begin{cases} \operatorname{curl}(\frac{1}{\mu_\alpha} \operatorname{curl} E_\alpha) - \omega^2 \varepsilon_\alpha E_\alpha = 0 & \text{in } \Omega, \\ E_\alpha \times \nu = g & \text{on } \partial\Omega, \end{cases}$$

with  $g$  a given datum on  $\partial\Omega$ .

The electric field denoted  $E_0$ , in the absence of all the imperfections, is such that:

$$(6) \quad \begin{cases} \operatorname{curl}(\frac{1}{\mu_0} \operatorname{curl} E_0) - \omega^2 \varepsilon_0 E_0 = 0 & \text{in } \Omega, \\ E_0 \times \nu = g & \text{on } \partial\Omega. \end{cases}$$

Let

$$H(\operatorname{curl}; \Omega) = \{u \in (L^2(\Omega))^3; \operatorname{curl} u \in (L^2(\Omega))^3\}$$

be endowed with its usual Hermitian product denoted here by  $(\cdot, \cdot)_{H(\operatorname{curl}; \Omega)}$ ; the corresponding norm is denoted by  $\|\cdot\|_{H(\operatorname{curl}; \Omega)}$ . By representing the surface divergence by  $\operatorname{div}_{\partial\Omega}$ , let us consider the space

$$TH^{-\frac{1}{2}}(\operatorname{div}; \partial\Omega) = \{q \in (H^{-\frac{1}{2}}(\partial\Omega))^3; \operatorname{div}_{\partial\Omega} q \in H^{-\frac{1}{2}}(\partial\Omega), q \cdot \nu = 0 \text{ on } \partial\Omega\},$$

with its usual norm denoted here by  $\|\cdot\|_{TH^{-\frac{1}{2}}(\operatorname{div}; \partial\Omega)}$ . The vector fields  $E_\alpha$  and  $E_0$ , satisfying (5) and (6) respectively, will be sought in  $H(\operatorname{curl}; \Omega)$ , and the datum  $g$  will be taken in  $TH^{-\frac{1}{2}}(\operatorname{div}; \partial\Omega)$ . For such a datum, let us consider  $u_g \in H(\operatorname{curl}; \Omega)$  such that (see e.g. [5]):

$$(7) \quad \begin{cases} u_g \times \nu = g & \text{on } \partial\Omega, \\ \|u_g\|_{H(\operatorname{curl}; \Omega)} \leq C_\Omega \|g\|_{TH^{-\frac{1}{2}}(\operatorname{div}; \partial\Omega)}, \end{cases}$$

where  $C_\Omega > 0$  is a constant depending only on  $\Omega$ . By setting

$$\mathcal{H} = \{u \in H(\operatorname{curl}; \Omega); u \times \nu = 0 \text{ on } \partial\Omega\},$$

a subspace endowed with  $(\cdot, \cdot)_{H(\operatorname{curl}; \Omega)}$ , and using the extension field  $u_g$ , the determination of  $E_\alpha$  satisfying (5) is reduced to the problem that consists of finding  $\mathcal{E}_\alpha \in \mathcal{H}$  such that:

$$(8) \quad \begin{aligned} & \int_\Omega \frac{1}{\mu_\alpha} \operatorname{curl} \mathcal{E}_\alpha \cdot \overline{\operatorname{curl} v} dx - \omega^2 \int_\Omega \varepsilon_\alpha \mathcal{E}_\alpha \cdot \overline{v} dx = \\ & - \int_\Omega \frac{1}{\mu_\alpha} \operatorname{curl} u_g \cdot \overline{\operatorname{curl} v} dx + \omega^2 \int_\Omega \varepsilon_\alpha u_g \cdot \overline{v} dx \quad \forall v \in \mathcal{H}. \end{aligned}$$

Also with the same extension field, the determination of  $E_0$  satisfying (6) is reduced to the one that consists of finding  $\mathcal{E}_0 \in \mathcal{H}$  such that:

$$(9) \quad \begin{aligned} & \int_{\Omega} \frac{1}{\mu_0} \operatorname{curl} \mathcal{E}_0 \cdot \overline{\operatorname{curl} v} \, dx - \omega^2 \int_{\Omega} \varepsilon_0 \mathcal{E}_0 \cdot \bar{v} \, dx = \\ & - \int_{\Omega} \frac{1}{\mu_0} \operatorname{curl} u_g \cdot \overline{\operatorname{curl} v} \, dx + \omega^2 \int_{\Omega} \varepsilon_0 u_g \cdot \bar{v} \, dx \quad \forall v \in \mathcal{H}. \end{aligned}$$

Of course, knowing  $u_g$ , while  $\mathcal{E}_\alpha$  and  $\mathcal{E}_0$  are in accordance with (8) and (9) respectively, we determine the physical fields:

$$(10) \quad E_\alpha := \mathcal{E}_\alpha + u_g, \quad E_0 := \mathcal{E}_0 + u_g.$$

**Remark 2.1.** *In the present framework, the essential hypothesis is that:  $k^2 = \omega^2 \mu_0 \varepsilon_0$  is taken such that (9) has a unique solution.*

The existence and uniqueness of the solution of (8) will be specified in the next section (see Theorem 3.1).

### 3. Asymptotic Formula for Perturbations

For measuring perturbations in the electric field due to the presence of imperfections, we consider here an analogous asymptotic expansion to the formula proposed by H. Ammari, M.S. Vogelius & D. Volkov [4]. Let us first introduce some additional notation and definitions. Let us consider, for  $x \neq z \in \mathbb{R}^3$ , the scalar function

$$\Phi^k(x, z) = \frac{e^{ik|x-z|}}{4\pi|x-z|},$$

with the constant  $k$  defined as in Remark 2.1. Of course,  $\Phi^k$  is a “free space” Green’s function for the Helmholtz operator  $\Delta + k^2$ , i.e., it satisfies:

$$(\Delta + k^2)\Phi^k(\cdot, z) = -\delta_z \quad \text{in } \mathbb{R}^3.$$

Let us now define the matrix valued function  $G(x, z)$ , for  $x \neq z \in \mathbb{R}^3$ , as

$$G(x, z) = -\mu_0(\Phi^k(x, z) \mathbf{I}_3 + \frac{1}{k^2} D_x^2 \Phi^k(x, z)),$$

where  $D_x^2$  denotes the Hessian, and  $G(x, z)$  is a “free space” Green’s function for the “background” electric problem:

$$\operatorname{curl}_x \left( \frac{1}{\mu_0} \operatorname{curl}_x G(x, z) \right) - \omega^2 \varepsilon_0 G(x, z) = -\delta_z \mathbf{I}_3.$$

The operator  $\operatorname{curl}_x$  applies here to matrices, column-by-column.

Let  $\{\gamma_n\}_{0 \leq n \leq m}$  be a set of complex constants with  $\operatorname{Re}(\gamma_n) > 0$ , for  $0 \leq n \leq m$ . Typically,  $\{\gamma_n\}_{0 \leq n \leq m}$  will be related to either the set  $\{\mu_n\}_{0 \leq n \leq m}$  or the set  $\{\varepsilon_n\}_{0 \leq n \leq m}$ . For any fixed  $1 \leq j_0 \leq m$ , let  $\gamma$  denote the function defined as:  $\forall x \in \mathbb{R}^3$ ,

$$\gamma(x) = \begin{cases} \gamma_0, & \text{if } x \in \mathbb{R}^3 \setminus \overline{B_{j_0}}, \\ \gamma_{j_0}, & \text{if } x \in B_{j_0}. \end{cases}$$

Let  $1 \leq l \leq 3$ . We denote by  $\phi_l$  the solution to the problem such that:

$$(11) \quad \left\{ \begin{array}{l} \operatorname{div}(\gamma_0 \operatorname{grad} \phi_l) = 0 \quad \text{in } \mathbb{R}^3 \setminus \overline{B_{j_0}}, \\ \operatorname{div}(\gamma_{j_0} \operatorname{grad} \phi_l) = 0 \quad \text{in } B_{j_0}, \\ \phi_l^+ - \phi_l^- = 0 \quad \text{on } \partial B_{j_0}, \\ \frac{\gamma_0}{\gamma_{j_0}} \left( \frac{\partial \phi_l}{\partial \nu} \right)^+ - \left( \frac{\partial \phi_l}{\partial \nu} \right)^- = 0 \quad \text{on } \partial B_{j_0}, \\ \phi_l(x) - x_l \rightarrow 0 \quad \text{as } |x| \rightarrow \infty. \end{array} \right.$$

In (11), the outward unit normal to  $B_{j_0}$ , defined on the boundary  $\partial B_{j_0}$  of  $B_{j_0}$ , is also denoted by  $\nu$ , and the superscripts  $+$ ,  $-$  indicate the limiting values as  $\partial B_{j_0}$  is approached from outside  $B_{j_0}$ , and from inside  $B_{j_0}$  respectively. As mentioned in [4], the existence and uniqueness of  $\phi_l$  can be established (in the real as well as in the complex case) by using single layer potentials with suitably chosen densities ([10], [12]). The function  $\phi_l$  depends only on  $\gamma_0$  and  $\gamma_{j_0}$  through the ratio  $c = \frac{\gamma_0}{\gamma_{j_0}}$ . Here, the essential assumption is that the constant  $c$  cannot be zero or a negative real number. With this aspect ratio, we define (as in [4]) the polarization tensor,  $M^{j_0}(c)$ , of the inhomogeneity  $B_{j_0}$  as follows:  $\forall 1 \leq i, l \leq 3$ ,

$$(12) \quad M_{il}^{j_0}(c) = c^{-1} \int_{B_{j_0}} \frac{\partial \phi_l}{\partial x_i} dx.$$

Following [4], the tensor  $M^{j_0}(c)$  is symmetric, and is furthermore positive definite if  $c \in \mathbb{R}_+^*$ .

Let us now reconsider the vector fields  $\mathcal{E}_\alpha, \mathcal{E}_0$  introduced from (8) - (9). Although these vector fields, as well as  $u_g$  given in (7), have been defined only in a weak sense on  $\partial\Omega$ , elliptic regularity results ensure that  $u_g, \mathcal{E}_\alpha, \mathcal{E}_0$  are infinitely smooth vector fields (when  $g$  is infinitely smooth) and therefore the term  $(\frac{1}{\mu_\alpha} \text{curl } E_\alpha - \frac{1}{\mu_0} \text{curl } E_0)|_{\partial\Omega}$  is infinitely smooth.

The framework of this paper is the main result proposed in [4]. We recall below this result reformulated now for measuring the perturbation  $(\frac{1}{\mu_\alpha} \text{curl } E_\alpha - \frac{1}{\mu_0} \text{curl } E_0) \times \nu|_{\partial\Omega}$ , in the tangential boundary trace of the curl of the electric field due to the presence of imperfections.

**Theorem 3.1.** *Let (2) be satisfied, and  $k^2 = \omega^2 \mu_0 \varepsilon_0$  be taken such that (9) has a unique solution. There exists  $\alpha_0 > 0$  such that, for a given  $g \in TH^{-\frac{1}{2}}(\text{div}; \partial\Omega)$  and any  $0 < \alpha < \alpha_0$ , the boundary value problem (5) has a unique (weak) solution. The constant  $\alpha_0$  depends on  $\{B_j\}_{1 \leq j \leq m}$ ,  $\Omega$ ,  $\{\mu_j\}_{0 \leq j \leq m}$ ,  $\{\varepsilon_j\}_{0 \leq j \leq m}$ ,  $\omega$ , and  $d_0$ , but is otherwise independent of the points  $z_j$ ,  $1 \leq j \leq m$ . Let  $E_\alpha$  denote the unique (weak) solution to (5), and let  $E_0$  be the unique (weak) solution to the boundary value problem (6) corresponding to the same  $g \in TH^{-\frac{1}{2}}(\text{div}; \partial\Omega)$ . For any  $z \in \partial\Omega$ , we then have:*

$$(13) \quad \begin{aligned} & (\frac{1}{\mu_\alpha} \text{curl } E_\alpha - \frac{1}{\mu_0} \text{curl } E_0)(z) \times \nu(z) \\ & - 2 \int_{\partial\Omega} \text{curl}_z(\Phi^k(x, z)) (\frac{1}{\mu_\alpha} \text{curl } E_\alpha - \frac{1}{\mu_0} \text{curl } E_0)(x) \times \nu(x) \times \nu(z) d\sigma_x = \\ & 2\alpha^3 \omega^2 \sum_{j=1}^m (\frac{\mu_0}{\mu_j} - 1) G(z_j, z) \times \nu(z) M^j(\frac{\mu_0}{\mu_j})(\text{curl } E_0)(z_j) + \\ & 2\alpha^3 \omega^2 \varepsilon_0 \sum_{j=1}^m (\frac{1}{\varepsilon_j} - \frac{1}{\varepsilon_0}) ((\text{curl}_x G)(z_j, z))^T \times \nu(z) M^j(\frac{\varepsilon_0}{\varepsilon_j}) E_0(z_j) + O(\alpha^4). \end{aligned}$$

The term  $O(\alpha^4)$  is bounded by  $C \alpha^4$ , uniformly in  $z$ . The positive constant  $C$  depends on  $\{B_j\}_{1 \leq j \leq m}$ ,  $\Omega$ ,  $\{\mu_j\}_{0 \leq j \leq m}$ ,  $\{\varepsilon_j\}_{0 \leq j \leq m}$ ,  $\omega$ ,  $\|g\|_{TH^{-\frac{1}{2}}(\text{div}; \partial\Omega)}$ , and  $d_0$ , but is otherwise independent of the points  $z_j$ ,  $1 \leq j \leq m$ .

It can now be specified in particular that the consideration of  $k^2$  such that the weak formulation (9) has a unique solution is also a hypothesis leading to the existence and uniqueness of the solution of the weak formulation (8).

In (13), and hereafter, the superscript “ $T$ ” denotes the transpose. The following result is a consequence of Theorem 3.1 and is presented in [4] as a basis for some approximate inversion techniques.

**Corollary 3.1.** *Let us consider the assumptions of Theorem 3.1, and denote by  $w$  any smooth vector-valued function such that:*

$$(14) \quad \operatorname{curl}(\operatorname{curl} w) - k^2 w = 0 \quad \text{in } W,$$

where  $W$  is an open neighborhood of  $\Omega$ . There exists a constant  $\alpha_0 > 0$  depending on  $\{B_j\}_{1 \leq j \leq m}$ ,  $\Omega$ ,  $\{\mu_j\}_{0 \leq j \leq m}$ ,  $\{\varepsilon_j\}_{0 \leq j \leq m}$ ,  $\omega$ , and  $d_0$ , but independent of  $w$ , of the points  $z_j$ ,  $1 \leq j \leq m$ , and such that for a given  $g \in TH^{-\frac{1}{2}}(\operatorname{div}; \partial\Omega)$  and any  $0 < \alpha < \alpha_0$ , the physical fields  $E_\alpha$  and  $E_0$  satisfy:

$$(15) \quad \int_{\partial\Omega} \operatorname{curl} E_\alpha \times \nu \cdot w \, d\sigma - \int_{\partial\Omega} \operatorname{curl} w \times \nu \cdot (\nu \times (E_\alpha \times \nu)) \, d\sigma = \\ \alpha^3 \sum_{j=1}^m \omega^2 \varepsilon_0 \mu_0 \left( \frac{\varepsilon_0}{\varepsilon_j} - 1 \right) \left[ M^j \left( \frac{\varepsilon_0}{\varepsilon_j} \right) E_0(z_j) \right] \cdot w(z_j) + \\ \alpha^3 \sum_{j=1}^m \left( \frac{\mu_0}{\mu_j} - 1 \right) \left[ M^j \left( \frac{\mu_0}{\mu_j} \right) \operatorname{curl} E_0(z_j) \right] \cdot \operatorname{curl} w(z_j) + O(\alpha^4).$$

This statement presents of course a version of the boundary perturbation in the curl of the electric field and appears well suited to applications since, as shown in [6], it allows us, with the help of inversion processes, to localize the imperfections by employing special test fields  $w$ .

#### 4. Numerical Discretizations

In numerical experiments of the localization of the imperfections, we will use the asymptotic formula (15) and therefore a discrete field associated with the solution of the weak formulation (8). In this part, we first describe a non-standard triangulation process of the domain  $\Omega$ . Then, with the help of a finite element method based on a mesh obtained from this process, we introduce the discrete formulation associated with (8).

**4.1. Preliminaries.** In order to simplify the presentation, we assume, in this section and in the following ones, that each imperfection present in the domain is a polyhedron. Usually, when we are concerned with the discretization of a non-homogeneous weak formulation, such as (8), we consider a mesh which implicitly takes into account the inhomogeneities of the domain. Typically, the conforming mesh of  $\Omega$  is made up of tetrahedra in such a way that the collection of tetrahedra associated with each imperfection covers entirely the geometry of the imperfection and constitutes in particular a conforming mesh of this imperfection. In general, this conforming mesh of  $\Omega$  results from a triangulation  $\mathcal{T}_\alpha$  of  $\Omega$  which is regular in the sense that there exists a constant  $c > 0$  such that  $\sup_{K \in \mathcal{T}_\alpha} \frac{h_K}{\varrho_K} \leq c$ , where  $h_K$  denotes the diameter of the tetrahedron  $K$  and  $\varrho_K$  is the diameter of the largest sphere included in  $K$ . By combining this conforming mesh of  $\Omega$  with edge elements (see Nédélec [18]), we can introduce (as in [6]) a discrete formulation associated with (8). Such a mesh will be called hereafter the *full finite element mesh* of  $\Omega$ . Since this mesh is as “fine” both inside and outside the smallest imperfection, we obtain, in the presence of a large number of small imperfections in  $\Omega$ , a far too large number of degrees of freedom associated with the above-mentioned discrete formulation — especially as this is a three-dimensional mesh and as mixed finite elements

are considered. As noticed in [6], this excessive number of degrees of freedom leads to some drawbacks in investigations regarding the numerical localization, as far as memory storage and CPU time are concerned.

Our attention in this paper being oriented towards the numerical simulations of the localization of very small imperfections, we will henceforth not consider full finite element meshes in our experiments.

**4.2. Discretization Process of the Domain.** We are interested in this subsection in a discretization process of the domain  $\Omega$  aimed at generating meshes that allow us to overcome the drawbacks inherent in the use of full finite element meshes. For the sake of simplicity in the presentation, let us assume here that  $\Omega$  contains only one imperfection, that is very small. Also,  $\Omega$  as well as the imperfection are polyhedral. The process starts by the construction of one tetrahedron (in  $\Omega$ ) surrounding the imperfection, and performs next a conforming discretization of the rest of the domain  $\Omega$  with tetrahedra as geometric elements. The tetrahedron surrounding the imperfection, called the *inhomogeneous tetrahedron*, is also a geometric element in this process. Typically, the collection  $\mathcal{T}$  formed by the inhomogeneous tetrahedron and by the tetrahedra of the rest of the domain constitutes a conforming mesh of  $\Omega$ , and must derive from a regular discretization in the sense that there exists a constant  $c > 0$  such that  $\sup_{K \in \mathcal{T}} \frac{h_K}{\varrho_K} \leq c$ , where  $h_K$  denotes the diameter of the tetrahedron  $K$  and  $\varrho_K$  is the diameter of the largest sphere included in  $K$ . The mesh size  $h$  of  $\Omega$ ,  $h = \sup_{K \in \mathcal{T}} h_K$ , depends in particular on the diameter of the inhomogeneous tetrahedron and therefore on  $\alpha^*$  the diameter of the imperfection. It is already important to mention that this mesh size can be reduced until a limiting value dependent on  $\alpha^*$ . Hereafter, such a conforming mesh of  $\Omega$  is called the *reduced mesh* of  $\Omega$ . This discretization process prohibits mesh sizes smaller than  $\alpha^*$  and accordingly any mesh which is too fine. Nevertheless, since we are concerned with an imperfection of very small diameter, the mesh size of  $\Omega$  can be taken as small as the size of a “fine” mesh of  $\Omega$  that could be considered in the absence of the imperfection.

By combining the reduced mesh of  $\Omega$  with edge elements, and with a composite integration method for taking into account the characteristics of the imperfection, we can introduce a discrete formulation associated with (8). Typically, the integration method is based on an integration mesh of the inhomogeneous tetrahedron and on the use of a composite numerical integration formula, for the calculation of any integral term (of the formulation) supported by this inhomogeneous tetrahedron. For suppleness of the implementation, the integration mesh is also constructed with tetrahedra. More precisely, this mesh is composed of two collections of tetrahedra covering in a conforming way the inhomogeneous tetrahedron: the set of tetrahedra covering in a conforming way the imperfection itself and the collection of tetrahedra outside the imperfection. It is already important to specify that there can exist large disproportions here between the volumes of tetrahedra inside and/or outside the imperfection.

Different reduced mesh “levels” can be built. In fact, from a homothetic transformation applied to the inhomogeneous tetrahedron of the initial reduced mesh, we obtain a new inhomogeneous tetrahedron with which we build a new reduced mesh of  $\Omega$  by performing the discretization process described previously. Typically, an isotropic shrinking of the inhomogeneous tetrahedron allows us to derive a reduced

mesh having a larger number of geometric elements in contrast with a reduced mesh based on a same balancing and deriving from an isotropic dilation of this inhomogeneous tetrahedron. A recursive construction of reduced meshes of  $\Omega$  can then be achieved by defining different reduced mesh levels in such a way that each level corresponds to a specific homothetic transformation of the initial inhomogeneous tetrahedron, and is hence associated with a specific reduced mesh. Three reduced mesh levels are illustrated in Figure 2 (with two-dimensional representations, where  $\Omega$  has the shape of the unit disk and contains one disk-like shaped imperfection of center  $(0.5, 0)^T$  and of 'radius' 0.02).

The stages of our approach are summarized as follows:

1. construct (in  $\Omega$ ) an inhomogeneous tetrahedron of diameter  $h_{K_0} > \alpha^*$ ,
2. perform the discretization of the rest of the domain  $\Omega$ , in order to obtain a reduced mesh of  $\Omega$ ,
3. construct an integration mesh of the inhomogeneous tetrahedron,
4. combine the reduced mesh with edge elements, and with the integration mesh, to introduce the discrete formulation associated with (8).

Of course, in the presence of multiple (polyhedral) imperfections, the same discretization process is also performed; an inhomogeneous tetrahedron is constructed for *each* imperfection and an integration mesh is associated with *each* inhomogeneous tetrahedron.

In Figure 2, illustrating both stages **1** and **2**, the edges of each inhomogeneous geometric element are represented in bold. The reduced mesh of the  $l$ th level contains more geometric elements than the reduced mesh of the  $(l + 1)$ th level, from a same balancing.

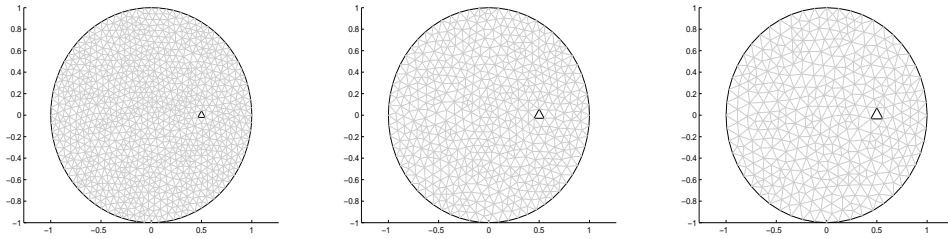


FIGURE 2. An illustration of three reduced mesh levels;  $l = 1$  (first level) on the left,  $l = 2$  in the middle, and  $l = 3$  on the right.

Figure 3 illustrates stage **3** and presents three integration meshes associated respectively with the three inhomogeneous geometric elements of the reduced meshes of Figure 2.

**4.3. Discrete Formulation.** For a reduced mesh of  $\Omega$ , of level  $l$ , we denote by  $h_l$  the corresponding mesh size and by  $\mathcal{T}_{h_l}$  the associated collection of tetrahedra. Let us assume that an integration mesh is systematically associated with each inhomogeneous tetrahedron of this reduced mesh, and is combined with a second-order accurate numerical integration formula. We use first order edge elements (see Nédélec [18]) for discretizing the formulation in electric field. By denoting by  $K$  a tetrahedron of  $\mathcal{T}_{h_l}$ , let us consider

$$R^1(K) = \{u : K \longrightarrow \mathbb{C}^3; \exists a, b \in \mathbb{C}^3, u(x) = a + b \times x, x = (x_1, x_2, x_3)^T \in K\}.$$

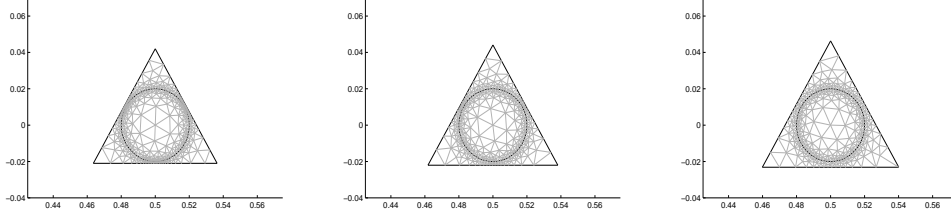


FIGURE 3. Representations of the integration meshes associated with the inhomogeneous geometric elements of the previous reduced meshes.

The discrete space associated with  $\mathcal{H}$  is given by

$$\mathcal{H}_{h_l} = \{u_{h_l} \in H(\text{curl}; \Omega); u_{h_l}|_K \in R^1(K) \ \forall K \in \mathcal{T}_{h_l}, u_{h_l} \times \nu = 0 \text{ on } \partial\Omega\},$$

and is also endowed, as was  $\mathcal{H}$ , with  $(\cdot, \cdot)_{H(\text{curl}; \Omega)}$ . The expression of any vector field of  $\mathcal{H}_{h_l}$  in each tetrahedron  $K \in \mathcal{T}_{h_l}$  can be written similarly as was done in [16] for  $\mathbb{R}^3$ -valued fields, in view of a practical implementation.

The discrete formulation associated with (8), and based on this reduced mesh, consists of finding  $\mathcal{E}_{h_l} \in \mathcal{H}_{h_l}$  such that:

$$(16) \quad \int_{\Omega} \frac{1}{\mu_{\alpha}} \text{curl } \mathcal{E}_{h_l} \cdot \overline{\text{curl } v_{h_l}} dx - \omega^2 \int_{\Omega} \varepsilon_{\alpha} \mathcal{E}_{h_l} \cdot \overline{v_{h_l}} dx = \\ - \int_{\Omega} \frac{1}{\mu_{\alpha}} \text{curl } u_g \cdot \overline{\text{curl } v_{h_l}} dx + \omega^2 \int_{\Omega} \varepsilon_{\alpha} u_g \cdot \overline{v_{h_l}} dx \ \forall v_{h_l} \in \mathcal{H}_{h_l}.$$

We mention that, due to the conforming finite element method used here, the proof of the existence and uniqueness of the solution of (8), given in [4], implies also (under the same hypotheses) the existence and uniqueness of the solution of the associated discrete formulation (16).

The matrix of the discrete system resulting from (16) is of a drastically reduced size, in contrast with the matrix of the system that would result from a discrete formulation based on a full finite element mesh of  $\Omega$  (built with a similar balancing), and is inverted with the help of a GMRES algorithm preconditioned by an incomplete **LU** factorization. We expect that the formulation (16) will allow us to achieve numerical simulations of the localization of imperfections with a saving of memory storage and reasonable CPU times, contrary to a discrete formulation based on a full finite element mesh.

## 5. Numerical Localization

This section is subdivided into four parts and deals with the effective localization of the imperfections in various contexts. We start by describing some computational configurations and are next concerned with numerical experiments based on three localization procedures. Each one of these procedures combines the asymptotic formula (15) with one of the following inversion processes: the Current Projection method, the MUSIC approach, or an Inverse Fourier method. Typically, four stages define each procedure. The first stage is that of the illumination of the domain from a well-chosen setting with incident waves. The second stage concerns the computation of the discrete electric field, through the formulation (16), and for each applied boundary current. The third stage makes use of both the asymptotic formula (15) and the discrete electric field, as well as particular test fields, for the

numerical evaluation of boundary measurements. The last stage is the application of the relevant inversion process.

In the second part of this section, we present the numerical results obtained from the procedure based on the Current Projection method, namely when the domain contains a single imperfection. The results of the localization of multiple imperfections are described in the third part of the section from the procedure based on the MUSIC approach, and in the last part of the section from the procedure now based on an Inverse Fourier method. As opposed to [6] where these procedures are introduced for achieving numerical localizations using full finite element meshes, we specify that only reduced meshes will be required here.

We already mention that the integration method that we use (in the computation of the discrete electric field or in the evaluation of boundary measurements) does not deteriorate the order of accuracy of the finite element discretization associated with each considered reduced mesh. Thus, the localization accuracy will only depend on this discretization order, besides the error inherent in the inversion procedure that is used.

**5.1. Computational Configurations.** Two distinct configurations of the (polyhedral) domain  $\Omega$ , having the diameter and the shape of the unit ball, are taken into account: the case where  $\Omega$  contains a single imperfection and when it contains multiple imperfections. For the first configuration, the single imperfection is a polyhedron having the shape of a ball of center  $(p_1, p_2, p_3)^T = (0.23, -0.31, 0.15)^T$  and of radius  $\alpha = 0.02$ . We perform, as described in Subsection 4.2, the discretization process of  $\Omega$  and retain for this configuration three reduced meshes obtained recursively. Namely, we denote by

- $\mathcal{T}_{h_1}$  the collection of tetrahedra corresponding to the initial reduced mesh of  $\Omega$ . This is a mesh built from an inhomogeneous tetrahedron of small diameter (approximately equal to  $5\alpha$ ), and identified hereafter as the reduced mesh of  $\Omega$  of first level ( $l = 1$ );
- $\mathcal{T}_{h_2}$  the collection of tetrahedra associated with the reduced mesh of  $\Omega$  of second level ( $l = 2$ ), built from a dilation of the initial inhomogeneous tetrahedron with a homothetic parameter equal to 1.05;
- $\mathcal{T}_{h_3}$  the collection of tetrahedra corresponding to the reduced mesh of  $\Omega$  of third level ( $l = 3$ ), also obtained from a dilation of the initial inhomogeneous tetrahedron but with a homothetic parameter now equal to  $(1.05)^2$ .

We have used more or less the same balancing (of the order of  $\frac{5}{2}$ ) in the construction of these reduced meshes and their sizes  $h_l$ ,  $1 \leq l \leq 3$ , are such that:  $h_1 < h_2 < h_3$ . In the following table, we give some characteristics of these meshes — denoting by  $NK$ ,  $NIE$ ,  $NIV$  the number of tetrahedra, internal edges and internal vertices respectively, as well by  $nf$ ,  $ne$  the number of boundary faces and boundary edges respectively.

	$NK$	$NIE$	$NIV$	$nf$	$ne$	$h_l$
$\mathcal{T}_{h_1}$	46402	51734	6969	3276	4914	0.17152
$\mathcal{T}_{h_2}$	31081	34252	4545	2750	4125	0.19100
$\mathcal{T}_{h_3}$	16021	17538	2309	1586	2379	0.22639

The discretization approach of Subsection 4.2 leads us to consider moreover, for each inhomogeneous tetrahedron present, a corresponding integration mesh. This is of course a conforming mesh for which large disproportions exist between the volumes

of tetrahedra inside and outside the imperfection. The collection of tetrahedra associated with the integration mesh of the inhomogeneous tetrahedron of  $\mathcal{T}_{h_l}$  ( $1 \leq l \leq 3$ ) is then not necessarily very large (about 1500 elements constitute each one of the three integration meshes considered here).

In the second configuration,  $\Omega$  contains more than one imperfection and each imperfection is a ball-like or ellipsoid-like shaped polyhedron. The collections of tetrahedra associated with the reduced meshes of  $\Omega$  are represented by

- $\mathcal{T}_h^4$  when  $\Omega$  contains three imperfections one of which has the shape of a ball of radius 0.016 and of center  $(0.23, -0.31, 0.15)^T$ . The second one is ellipsoid-shaped, centered at  $(-0.17, -0.43, -0.11)^T$  with 'semi-axes' of lengths 0.016, 0.016, 0.018 in the directions  $Ox$ ,  $Oy$ ,  $Oz$  respectively. The last imperfection is also ellipsoid-shaped, but centered at  $(-0.5, 0.25, 0.1)^T$  with the 'semi-axes' (on  $Oxy$ ) rotated about  $Oz$  by an angle of  $\frac{\pi}{4}$ . The lengths of the 'semi-axes' of this imperfection are 0.016, 0.017 and 0.019. We denote in this case by  $\alpha$  ( $\alpha = 0.019$ ) the maximal value of the semi-axes lengths and the 'radius' of the first imperfection;
- $\mathcal{T}_h^5$  when  $\Omega$  contains five imperfections, where each one has the shape of a ball of radius 0.01. We set here:  $\alpha = 0.01$ . These imperfections are respectively centered at  $(0, 0, 0)^T$ ,  $(0.25, 0.25, 0.25)^T$ ,  $(0.5, 0.5, 0.5)^T$ ,  $(-0.25, -0.25, -0.25)^T$ , and  $(-0.5, -0.5, -0.5)^T$ .

For this multiple imperfections context, we retain thus two reduced meshes of  $\Omega$ , where each mesh corresponds to a specific physical setting. The mesh size, denoted here by  $h$ , differs of course depending on whether we are concerned with  $\mathcal{T}_h^4$  or  $\mathcal{T}_h^5$ . We also mention that neither of these meshes is linked to any of the previous meshes of the single imperfection configuration, in the sense that any inhomogeneous tetrahedron of  $\mathcal{T}_h^4$  or of  $\mathcal{T}_h^5$  is not built from that of  $\mathcal{T}_{h_1}$ . Using the same notation as above, we give in the following table some characteristics of the two reduced meshes with multiple imperfections.

	$NK$	$NIE$	$NIV$	$nf$	$ne$	$h$
$\mathcal{T}_h^4$	66347	74349	10085	4168	6252	0.14546
$\mathcal{T}_h^5$	77263	86614	11753	4806	7209	0.13951

Of course, as previously for the single imperfection configuration, an integration mesh is systematically associated here with each inhomogeneous tetrahedron of  $\mathcal{T}_h^4$  and  $\mathcal{T}_h^5$ . We distinguish thus three integration meshes associated with the three inhomogeneous tetrahedra of  $\mathcal{T}_h^4$ , whereas we retain a unique integration mesh in the case of the inhomogeneous tetrahedra of  $\mathcal{T}_h^5$  (all the imperfections having here both the same shape and size, and the same type of tetrahedron being used to surround each imperfection — the inhomogeneous tetrahedra have a unique shape and identical diameters).

As opposed to the context of full finite element meshes, the mesh size  $h_l$  or  $h$  resulting from each reduced mesh is systematically larger than the largest of the diameters and 'axes lengths' of the imperfections:  $h_l, h > 2\alpha$ .

In the construction of the reduced meshes associated with  $\mathcal{T}_h^4$  and  $\mathcal{T}_h^5$ , we have used more or less the same balancing (of the order of  $\frac{5}{2}$  as before). With such a balancing, the usual discretization process of the domain results in a full mesh having an exorbitant number of tetrahedra, in each one of the previous settings (for example, more than 1 140 000 tetrahedra result from the full mesh of the domain,

with approximately 0.0619 as mesh size, when it contains a single imperfection of 'radius' 0.08 only!). Let us mention also that, by using similar balancings in the constructions of meshes, a reduced mesh of the domain containing multiple imperfections (with  $\alpha$  the common order of magnitude of their diameters) does not necessarily have a larger number of tetrahedra than a reduced mesh of the same domain with a single imperfection (with an order of magnitude of its diameter close to  $\alpha$ ).

Let us specify that in comparison with the imperfections considered in [6], those present in the above configurations are one order of magnitude smaller.

**5.2. From a Procedure based on a Current Projection Method.** We describe in this subsection the results obtained from a localization procedure uniquely devoted to the case where the domain contains a single imperfection. This procedure, combining the asymptotic formula (15) and a Current Projection method, is presented in [6] and is aimed at determining the center of the imperfection. To begin, let us recall briefly how the formula (15) is used. We denote by  $p = (p_1, p_2, p_3)^T$  the center of the imperfection, by  $M$  its "rescaled" polarization tensor  $(\frac{\mu_0}{\mu_1} - 1)M^1(\frac{\mu_0}{\mu_1})$ , and by  $N$  its other "rescaled" polarization tensor  $(\frac{\epsilon_0}{\epsilon_1} - 1)M^1(\frac{\epsilon_0}{\epsilon_1})$ . When we neglect the asymptotically small remainder term in (15), it follows that:

$$(17) \quad \Gamma := \int_{\partial\Omega} \text{curl } E_\alpha \times \nu \cdot w \, d\sigma - \int_{\partial\Omega} \text{curl } w \times \nu \cdot (\nu \times g) \, d\sigma \approx \alpha^3 k^2 (N E_0(p)) \cdot w(p) + \alpha^3 (M \text{curl } E_0(p)) \cdot \text{curl } w(p),$$

with  $w$  any smooth vector-valued function satisfying

$$\text{curl}(\text{curl } w) - k^2 w = 0 \quad \text{in } W,$$

where  $W$  is an open neighborhood of  $\Omega$ .

According to (10), we recall that  $E_\alpha = \mathcal{E}_\alpha + u_g$ , where  $\mathcal{E}_\alpha$  is the solution to (8). The datum  $g$  in (7), that defines  $u_g$ , is considered from a physical point of view as a current applied on  $\partial\Omega$ . The discrete field  $\mathcal{E}_h$  associated with  $\mathcal{E}_\alpha$  is the solution of the discrete formulation (16), and the discrete electric field associated with  $E_\alpha$  is defined as:  $E_\alpha^h := \mathcal{E}_h + u_g$ . The inversion process is established by using in (17) particular currents as well as special test fields, and by evaluating the corresponding numerical measurements from the left-hand side of (17).

We apply different currents for  $g$  that correspond to the following background vector potentials

$$E_0^{(1)}(x) = \begin{pmatrix} 0 \\ 0 \\ e^{ikx_2} \end{pmatrix}, \quad E_0^{(2)}(x) = \begin{pmatrix} e^{ikx_3} \\ 0 \\ 0 \end{pmatrix}, \quad E_0^{(3)}(x) = \begin{pmatrix} 0 \\ e^{ikx_1} \\ 0 \end{pmatrix},$$

$x = (x_1, x_2, x_3)$ , and evaluate from the left-hand side of (17) the terms  $\Gamma_{(j,i)}$ ,  $1 \leq i, j \leq 3$ , defined as:

$$(18) \quad \Gamma_{(j,i)} := \int_{\partial\Omega} \text{curl } E_{\alpha,(i)}^h \times \nu \cdot w^{(j,i)} \, d\sigma - \int_{\partial\Omega} \text{curl } w^{(j,i)} \times \nu \cdot (\nu \times g^{(i)}) \, d\sigma.$$

Namely, for each current  $g^{(i)} = E_0^{(i)} \times \nu$ , we put  $g := g^{(i)}$  in (7) in order to compute by (16) the corresponding discrete electric field denoted here by  $E_{\alpha,(i)}^h$ , and consider

the test vector fields

$$\begin{aligned}
w^{(1,1)}(x) &= \begin{pmatrix} 0 \\ 0 \\ e^{-ikx_2} \end{pmatrix}, & w^{(2,1)}(x) &= \begin{pmatrix} e^{-ikx_2} \\ 0 \\ 0 \end{pmatrix}, & w^{(3,1)}(x) &= \begin{pmatrix} 0 \\ 0 \\ e^{ikx_2} \end{pmatrix}, \\
w^{(1,2)}(x) &= \begin{pmatrix} e^{-ikx_3} \\ 0 \\ 0 \end{pmatrix}, & w^{(2,2)}(x) &= \begin{pmatrix} 0 \\ e^{-ikx_3} \\ 0 \end{pmatrix}, & w^{(3,2)}(x) &= \begin{pmatrix} e^{ikx_3} \\ 0 \\ 0 \end{pmatrix}, \\
w^{(1,3)}(x) &= \begin{pmatrix} 0 \\ e^{-ikx_1} \\ 0 \end{pmatrix}, & w^{(2,3)}(x) &= \begin{pmatrix} 0 \\ 0 \\ e^{-ikx_1} \end{pmatrix}, & w^{(3,3)}(x) &= \begin{pmatrix} 0 \\ e^{ikx_1} \\ 0 \end{pmatrix}.
\end{aligned}$$

Each  $\Gamma_{(j,i)}$ ,  $1 \leq i, j \leq 3$ , is called the *numerical boundary measurement*. It follows from the formula (17) and with these considerations that:

$$(19) \quad \left\{ \begin{array}{l} \Gamma_{(1,1)} \approx \alpha^3 k^2 N_{33} + \alpha^3 k^2 M_{11}, \\ \Gamma_{(2,1)} \approx \alpha^3 k^2 N_{13} - \alpha^3 k^2 M_{31}, \\ \Gamma_{(3,1)} \approx (\alpha^3 k^2 N_{33} - \alpha^3 k^2 M_{11}) e^{2ikp_2}, \\ \Gamma_{(1,2)} \approx \alpha^3 k^2 N_{11} + \alpha^3 k^2 M_{22}, \\ \Gamma_{(2,2)} \approx \alpha^3 k^2 N_{21} - \alpha^3 k^2 M_{12}, \\ \Gamma_{(3,2)} \approx (\alpha^3 k^2 N_{11} - \alpha^3 k^2 M_{22}) e^{2ikp_3}, \\ \Gamma_{(1,3)} \approx \alpha^3 k^2 N_{22} + \alpha^3 k^2 M_{33}, \\ \Gamma_{(2,3)} \approx \alpha^3 k^2 N_{32} - \alpha^3 k^2 M_{23}, \\ \Gamma_{(3,3)} \approx (\alpha^3 k^2 N_{22} - \alpha^3 k^2 M_{33}) e^{2ikp_1}, \end{array} \right.$$

where the terms  $M_{ij}$  and  $N_{ij}$ ,  $1 \leq i, j \leq 3$ , are respectively the coefficients of  $M$  and  $N$ . As specified in [6], the measurements  $\Gamma_{(1,i)}$ ,  $\Gamma_{(2,i)}$ ,  $1 \leq i \leq 3$ , in (19), allow us to provide an approximation of the rescaled tensor  $\alpha^3 k^2 M$  or  $\alpha^3 k^2 N$  depending on whether  $\varepsilon_1 = \varepsilon_0$  or  $\mu_1 = \mu_0$ . Once an approximation of the tensor  $\alpha^3 k^2 M$  or  $\alpha^3 k^2 N$  is determined, we can localize the center of the imperfection from the measurements  $\Gamma_{(3,i)}$ ,  $1 \leq i \leq 3$ , in (19), for certain values of  $k$  and when  $\mu_0 > 0$ ,  $\mu_1 > 0$ ,  $\varepsilon_0 > 0$ ,  $\varepsilon_1 > 0$ .

We mention that the measurements in (19) are not however sufficient to determine the approximations of  $\alpha^3 k^2 M$  and  $\alpha^3 k^2 N$  in the general case, where both  $\mu_1 \neq \mu_0$  and  $\varepsilon_1 \neq \varepsilon_0$ .

When the rescaled polarization tensors  $(\frac{\mu_0}{\mu_1} - 1)M^1(\frac{\mu_0}{\mu_1})$  and  $(\frac{\varepsilon_0}{\varepsilon_1} - 1)M^1(\frac{\varepsilon_0}{\varepsilon_1})$  are known, an approximation of the order of magnitude of the diameter of the imperfection can be determined from one of the measurements  $\Gamma_{(1,i)}$ ,  $1 \leq i \leq 3$ , even if  $\mu_1 \neq \mu_0$  and  $\varepsilon_1 \neq \varepsilon_0$ , with of course  $\mu_0 > 0$ ,  $\mu_1 > 0$ ,  $\varepsilon_0 > 0$ ,  $\varepsilon_1 > 0$ . Following [6], we determine the approximations of  $M^1(\frac{\mu_0}{\mu_1})$  and  $M^1(\frac{\varepsilon_0}{\varepsilon_1})$  without any relation to reduced meshes. In fact, the evaluation of  $M^1(\frac{\mu_0}{\mu_1})$ , or  $M^1(\frac{\varepsilon_0}{\varepsilon_1})$ , is done by calculating numerically the coefficients of the tensor from (12), with  $B_{j_0} \equiv B_1$  identified then with a polyhedral domain having here the shape and the diameter of the unit ball, and after discretizing the scalar potential, solution of (11), from the combination of a standard finite element mesh with interior nodal finite

elements and boundary finite elements of first-order (see also e.g. [16] for such a combination). Another approach, entirely based on integral equation techniques, for computing numerically the solution of (11), is the one resulting from [19].

In what follows, we fix  $\mu_0 = \varepsilon_0 = 1$ , and present the numerical results of the localization of a single imperfection contained in  $\Omega$ . We make use of (19) by distinguishing the cases:  $\mu_1 = \mu_0$  with  $\varepsilon_1 \neq \varepsilon_0$ , as well as  $\mu_1 \neq \mu_0$  with  $\varepsilon_1 = \varepsilon_0$ . Here and in the following subsections, all our numerical results will be described with respect to the parameter

$$(20) \quad \tau := \alpha \omega.$$

Let us mention that this parameter would be defined as  $\tau := \alpha \omega / r$  if  $\Omega$  was a ball (or ball-like) of radius  $r$ . Based on the numerical study of the asymptotic formula (13) done in [6], each considered frequency must be such that  $k$  is in accordance with Remark 2.1, and must not lead to a too small or a large value of  $\tau$  ( $\tau < 1$ ). Consequently, we will not use here frequencies that are too high and each considered frequency will be such that  $k < \frac{\pi}{2}$  for example, in the case of the reconstruction of the center of the imperfection in  $\Omega$  (domain having here the diameter and the shape of the unit ball).

We respectively denote by  $\frac{|\alpha - \alpha_h|}{|\alpha|}$ ,  $\frac{|p - p_h|_{\mathbb{R}^3}}{|p|_{\mathbb{R}^3}}$ , where  $|\cdot|_{\mathbb{R}^3}$  is the infinity norm on  $\mathbb{R}^3$ , the relative errors on the 'radius'  $\alpha$  and the center  $p$  of the imperfection, when  $\alpha_h$ ,  $p_h$  are the 'radius' and the center of the localized imperfection.

Figures 4 - 5 present results obtained from  $\mathcal{T}_{h_l}$ ,  $1 \leq l \leq 3$ , with  $\mu_1 = 1$ ,  $\varepsilon_1 = 3, 5, 10$ . We observe an asymptotic behaviour of the relative error on the 'radius' of the imperfection with respect to  $\tau$ .

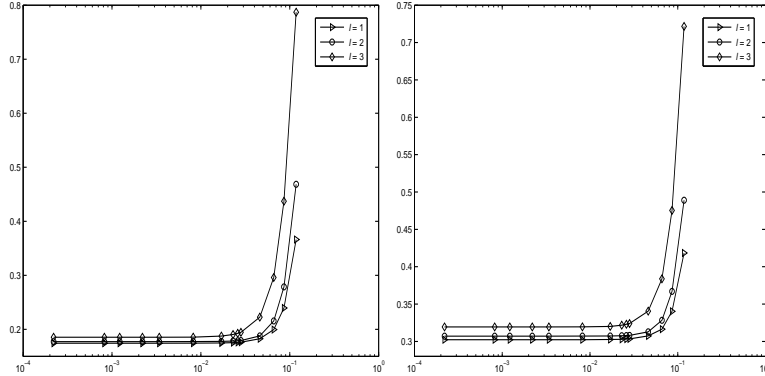


FIGURE 4. Semi-log representation of the relative error on the radius with respect to some values of  $\tau$ , for  $\mu_1 = 1$  with  $\varepsilon_1 = 3$  (at left) and  $\varepsilon_1 = 5$  (at right), from  $\mathcal{T}_{h_l}$ ,  $1 \leq l \leq 3$ .

We observe in the case where  $\mu_1 = 1$  that the relative error on the radius increases with respect to  $\tau$ , independently of the considered reduced mesh. On the other hand, for a large range of values of  $\tau$ , this relative error increases with respect to the contrast of the domain. Figures 4 - 5 show moreover that this relative error becomes more important when we augment the reduced mesh level and that, for the low contrasts, the two first reduced mesh levels lead to errors on the radius that are not very different for a large range of values of  $\tau$ .

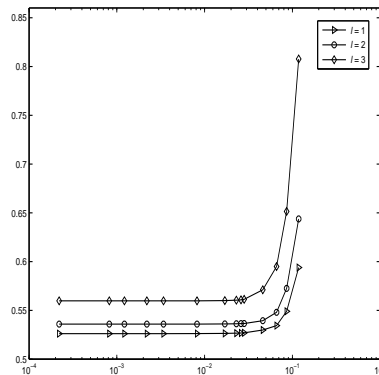


FIGURE 5. Semi-log representation of the relative error on the radius with respect to some values of  $\tau$ , for  $\mu_1 = 1$  with  $\varepsilon_1 = 10$  from  $\mathcal{T}_{h_l}$ ,  $1 \leq l \leq 3$ .

We mention that an asymptotic behaviour of the relative error on the radius, with respect to  $\tau$ , is also observed from simulations in the case where  $\mu_1 = 3, 5, 10$  with  $\varepsilon_1 = 1$ . For a range of values of  $\tau$  ( $\tau \ll 10^{-1}$ ), this relative error increases slightly when the contrast becomes important. We observe from experiments, for  $\varepsilon_1 = 1$  and for such values of  $\tau$ , that the relative error on the radius is asymptotically slightly more accurate than the one obtained by taking  $\mu_1 = 1$ , independently of the considered reduced mesh.

In the case of low contrasts, we represent in Figures 6 - 7 the cross-sections at  $x = p_1$ ,  $y = p_2$  and  $z = p_3$ , of the original imperfection (with center  $(p_1, p_2, p_3)^T$ ) and of the reconstructed imperfection resulting from the first level of the reduced mesh.

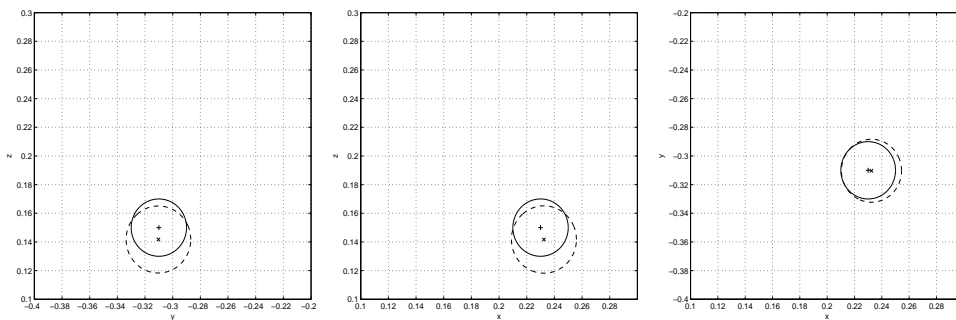


FIGURE 6. Respective cross-sections at  $x = p_1$ ,  $y = p_2$  and  $z = p_3$ , from  $\mathcal{T}_{h_1}$  and with  $\mu_1 = 1$ ,  $\varepsilon_1 = 3$ ,  $\tau = 1.7 \cdot 10^{-2}$ . Superposition of the original imperfection (—) whose center is marked by “+”, and of the reconstructed imperfection (---) with its center marked by “×”.

As indicated in Figure 8, we observe from simulations an asymptotic behaviour of the relative error on the center of the imperfection with respect to  $\tau$ , independently of the considered reduced mesh and when  $\mu_1 = 1$ . On the other hand, this relative error varies with respect to the contrast of the domain and it appears, contrary to

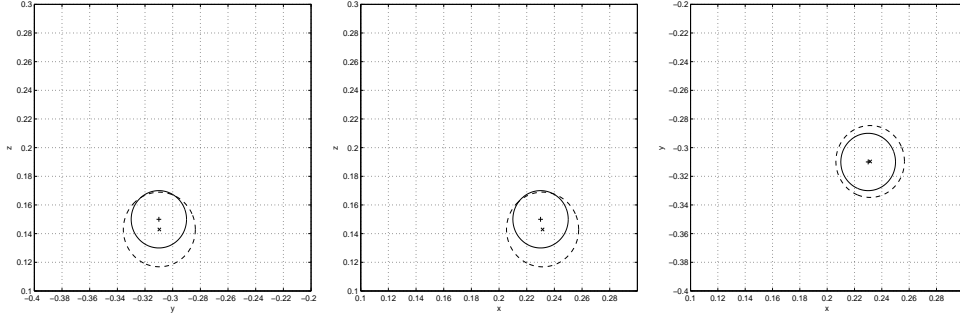


FIGURE 7. Respective cross-sections at  $x = p_1$ ,  $y = p_2$  and  $z = p_3$ , from  $\mathcal{T}_{h_1}$  and with  $\mu_1 = 1$ ,  $\varepsilon_1 = 5$ ,  $\tau = 2.6 \cdot 10^{-2}$ . Superposition of the original imperfection (—) whose center is marked by “+”, and of the reconstructed imperfection (---) with its center marked by “x”.

the error on the radius, that it does not systematically increase significantly (for a large range of values of  $\tau$ ) when we augment the reduced mesh level or when the contrast of the domain increases. Also, from experiments we observe that the relative error on the center, when  $\varepsilon_1 = 1$ , is not systematically more accurate than the one obtained by taking  $\mu_1 = 1$ , independently of the considered reduced mesh.

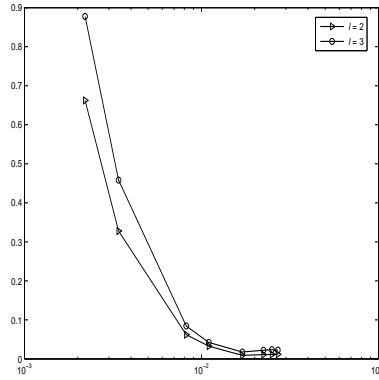


FIGURE 8. Semi-log representation of the relative error on the center with respect to some values of  $\tau$ , from  $\mathcal{T}_{h_2}$  ( $\text{---}\blacktriangleright\text{---}$ ) and  $\mathcal{T}_{h_3}$  ( $\text{---}\circ\text{---}$ ), for  $\mu_1 = 1$  with  $\varepsilon_1 = 10$ .

The behaviours of the relative errors on the radius and the center, with respect to  $\tau$ , indicate to us that accurate reconstructions of the imperfection cannot be expected in the case of too small or large values of  $\tau$ . Moreover, it appears more efficient to consider, in simulations, the second level of the reduced mesh instead of the first level due to a more reasonable CPU time and the fact that the relative errors obtained from  $\mathcal{T}_{h_2}$  are not numerically very different from those resulting from  $\mathcal{T}_{h_1}$ , for a large range of values of  $\tau$ . On the other hand, since the relative errors on the radius from  $\mathcal{T}_{h_2}$  are significantly better than those obtained from  $\mathcal{T}_{h_3}$ , we present below the results of experiments based mainly on  $\mathcal{T}_{h_2}$ .

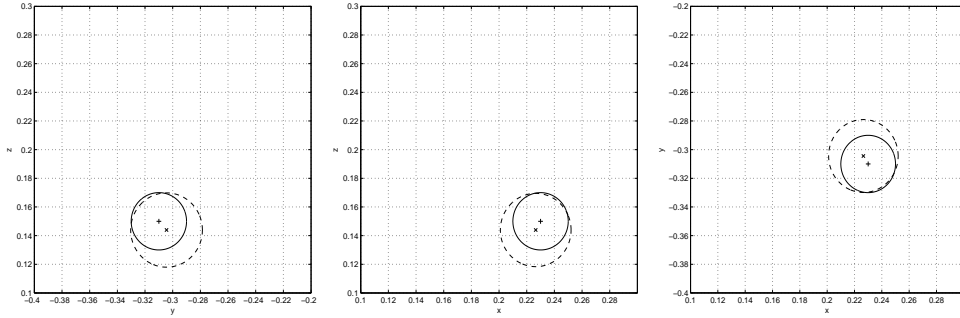


FIGURE 9. Respective cross-sections at  $x = p_1$ ,  $y = p_2$  and  $z = p_3$ , from  $\mathcal{T}_{h_2}$  and with  $\mu_1 = 1$ ,  $\varepsilon_1 = 5$ ,  $\tau = 2.6 \cdot 10^{-2}$ . Superposition of the original imperfection (—) whose center is marked by “+”, and of the reconstructed imperfection (---) with its center marked by “x”.

Figure 9 allows us to notice that the imperfection reconstructed from  $\mathcal{T}_{h_2}$  is of similar size to the one of the imperfection reconstructed from  $\mathcal{T}_{h_1}$  (see Figure 7), at the same frequency and for the same contrast, but has a slightly different center.

The results represented in Figure 10 are obtained for a stronger contrast and at a lower frequency. As opposed to this case where  $\mu_1 = 1$  with  $\varepsilon_1 = 10$ , the

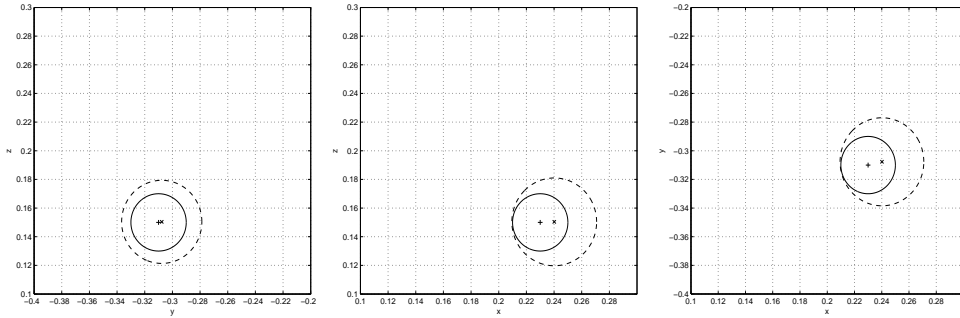


FIGURE 10. Respective cross-sections at  $x = p_1$ ,  $y = p_2$  and  $z = p_3$ , from  $\mathcal{T}_{h_2}$  and with  $\mu_1 = 1$ ,  $\varepsilon_1 = 10$ ,  $\tau = 1.17 \cdot 10^{-2}$ . Superposition of the original imperfection (—) whose center is marked by “+”, and of the reconstructed imperfection (---) with its center marked by “x”.

reconstructed imperfection at the same frequency and when  $\mu_1 = 10$  with  $\varepsilon_1 = 1$  is of smaller size.

In comparison with the results of Figure 9, the reconstructed imperfection in Figure 10 is of larger size and its center is less accurate. We also notice from simulations with  $\mathcal{T}_{h_2}$  that the localization of the imperfection becomes in fact less accurate, when using the same contrast as before in Figure 9, but in the case where  $\tau = 1.17 \cdot 10^{-2}$ .

By reducing (again) the frequency, we obtain the results represented in Figure 11 - 12, from the same reduced mesh level and with different contrasts.

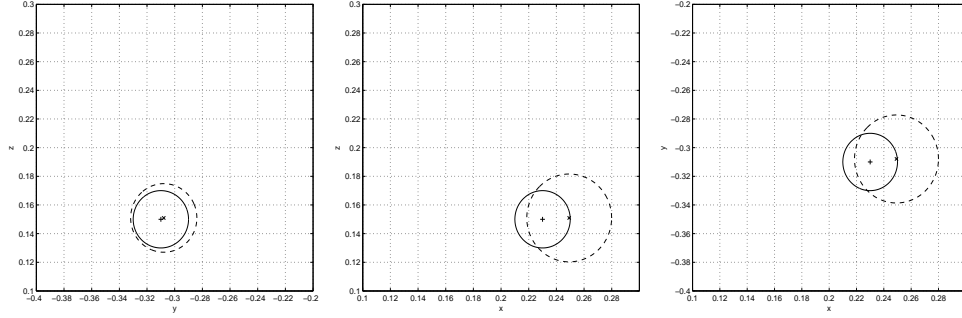


FIGURE 11. Respective cross-sections at  $x = p_1$ ,  $y = p_2$  and  $z = p_3$ , from  $\mathcal{T}_{h_2}$  and with  $\mu_1 = 1$ ,  $\varepsilon_1 = 10$ ,  $\tau = 8.2 \cdot 10^{-3}$ . Superposition of the original imperfection (—) whose center is marked by “+”, and of the reconstructed imperfection (---) with its center marked by “x”.

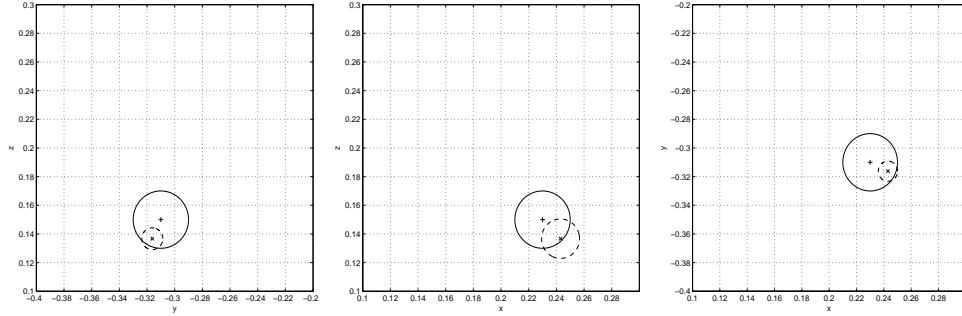


FIGURE 12. Respective cross-sections at  $x = p_1$ ,  $y = p_2$  and  $z = p_3$ , from  $\mathcal{T}_{h_2}$  and with  $\mu_1 = 10$ ,  $\varepsilon_1 = 1$ ,  $\tau = 8.2 \cdot 10^{-3}$ . Superposition of the original imperfection (—) whose center is marked by “+”, and of the reconstructed imperfection (---) with its center marked by “x”.

Similar results have been obtained from simulations with the same frequency, but for  $\mu_1 = 5$  with  $\varepsilon_1 = 1$ , and when  $\mu_1 = 1$  with  $\varepsilon_1 = 5$ . It appears that the localization of the imperfection becomes more and more inaccurate when the frequency decreases, and that following the case where  $\mu_1 = 1$  or  $\varepsilon_1 = 1$ , the reconstructed imperfection is of larger or smaller size respectively.

**5.3. From a Procedure based on the MUSIC Approach.** We describe in this subsection the numerical results obtained from a procedure aimed at localizing a single imperfection as well as multiple imperfections. This procedure, presented in [6], also makes use of the asymptotic formula (15), but now in combination with the Multiple Signal Classification (MUSIC) approach [1]. Before describing the numerical results, let us recall briefly how the MUSIC approach is applied, for simplicity, when  $\Omega$  represents the unit ball. Let  $(\theta_1, \dots, \theta_n) \in (S^2)^n$  be  $n$  directions of incidence, and denote by  $(\hat{x}_1, \dots, \hat{x}_n)$ ,  $n$  directions of observation, where  $\hat{x}_l = \theta_l^\perp$  for  $l = 1, \dots, n$ . Here, the essential assumption is that  $n$  is bigger than  $m$ , the number of imperfections. By neglecting the asymptotically small remainder term

in (15), we get:

$$(21) \quad \int_{\partial\Omega} \operatorname{curl} E_\alpha \times \nu \cdot w \, d\sigma - \int_{\partial\Omega} \operatorname{curl} w \times \nu \cdot (\nu \times g) \, d\sigma \approx \\ \alpha^3 \sum_{j=1}^m k^2 \left( \frac{\varepsilon_0}{\varepsilon_j} - 1 \right) \left[ M^j \left( \frac{\varepsilon_0}{\varepsilon_j} \right) E_0(z_j) \right] \cdot w(z_j) + \\ \alpha^3 \sum_{j=1}^m \left( \frac{\mu_0}{\mu_j} - 1 \right) \left[ M^j \left( \frac{\mu_0}{\mu_j} \right) \operatorname{curl} E_0(z_j) \right] \cdot \operatorname{curl} w(z_j),$$

where  $g$  is defined as in (7), and  $E_\alpha$  is determined through the solution  $\mathcal{E}_\alpha$  of (8).

Let us apply different currents for  $g$  that correspond to the background vector potentials  $E_{0,(l)}(x) = \theta_l^\perp e^{ik\theta_l \cdot x}$ ,  $1 \leq l \leq n$ . From each applied current  $g^{(l)} = E_{0,(l)} \times \nu$ ,  $1 \leq l \leq n$ , we take  $g := g^{(l)}$  in (7) and compute through (16) the corresponding discrete electric field denoted by  $E_{\alpha,(l)}^h$ . Now with the test vector field  $w^{(l')}(x) = \theta_{l'}^\perp e^{ik\theta_{l'} \cdot x}$ ,  $1 \leq l' \leq n$ , we evaluate from the left-hand side of (21) the term defined as follows,

$$A_{ll'} := \int_{\partial\Omega} \operatorname{curl} E_{\alpha,(l)}^h \times \nu \cdot w^{(l')} \, d\sigma - \int_{\partial\Omega} \operatorname{curl} w^{(l')} \times \nu \cdot (\nu \times g^{(l)}) \, d\sigma,$$

that denotes a numerical boundary measurement. In this way we build numerically the matrix  $A := (A_{ll'})_{1 \leq l, l' \leq n}$ . With these particular choices of background vector potentials and test vector fields, we get from the right-hand side of (21):

$$\alpha^3 \sum_{j=1}^m \left[ k^2 \left( \frac{\varepsilon_0}{\varepsilon_j} - 1 \right) \left( M^j \left( \frac{\varepsilon_0}{\varepsilon_j} \right) \theta_l^\perp \right) \cdot \theta_{l'}^\perp - \right. \\ \left. k^2 \left( \frac{\mu_0}{\mu_j} - 1 \right) \left( M^j \left( \frac{\mu_0}{\mu_j} \right) (\theta_l \times \theta_l^\perp) \right) \cdot (\theta_{l'} \times \theta_{l'}^\perp) \right] e^{ik(\theta_l + \theta_{l'}) \cdot z_j}.$$

If we replace the approximation in (21) by an equality, we may respectively write the coefficients of  $A$  as below, when all the imperfections are uniquely electric or uniquely magnetic: for  $1 \leq l, l' \leq n$ ,

$$A_{ll'} = \alpha^3 \sum_{j=1}^m k^2 \left( \frac{\varepsilon_0}{\varepsilon_j} - 1 \right) \left( M^j \left( \frac{\varepsilon_0}{\varepsilon_j} \right) \theta_l^\perp \right) \cdot \theta_{l'}^\perp e^{ik(\theta_l + \theta_{l'}) \cdot z_j},$$

or

$$A_{ll'} = -\alpha^3 \sum_{j=1}^m k^2 \left( \frac{\mu_0}{\mu_j} - 1 \right) \left( M^j \left( \frac{\mu_0}{\mu_j} \right) (\theta_l \times \theta_l^\perp) \right) \cdot (\theta_{l'} \times \theta_{l'}^\perp) e^{ik(\theta_l + \theta_{l'}) \cdot z_j}.$$

Let us consider some constant vector  $c \in \mathbf{R}^3$ , and set  $A^* = \overline{A}^T$ . Depending on whether all the imperfections are electric or magnetic, let us define, respectively for  $z \in \Omega$ ,

$$g_{z,c} := (c \cdot \theta_1^\perp e^{ik\theta_1 \cdot z}, \dots, c \cdot \theta_n^\perp e^{ik\theta_n \cdot z})^T,$$

where  $c$  is such that  $c \cdot \theta_l^\perp \neq 0$ , for all  $l = 1, \dots, n$ , or

$$g_{z,c} := (c \cdot (\theta_1 \times \theta_1^\perp) e^{ik\theta_1 \cdot z}, \dots, c \cdot (\theta_n \times \theta_n^\perp) e^{ik\theta_n \cdot z})^T,$$

with here  $c$  such that  $c \cdot (\theta_l \times \theta_l^\perp) \neq 0$ , for all  $l = 1, \dots, n$ .

Referring now to [1], it can be shown that there exists  $n_0 \in \mathbb{N}$  such that for any  $n \geq n_0$ ,

$$g_{z,c} \in \operatorname{Range}(AA^*) \text{ if and only if } z \in \{z_1, \dots, z_m\}.$$

An application of the singular-value decomposition of  $A$  is the determination of the number of imperfections, since the number of significant singular-values of  $A$  yields

the number of detectable imperfections (see [1], [2]). Typically, if there exist  $3m$  significant singular-values of  $A$ , then there are  $m$  detectable imperfections. If all the singular-values of  $A$  are zero or close to zero (when  $A$  does not have any significant singular-value), then there are no detectable imperfections in the domain.

In the case where there are detectable imperfections in the domain, we can make use of the singular-vectors of  $A$  to locate them. If we call  $V_S = [u_1, u_2, \dots, u_{n^*}]$  the matrix block built with significant left singular-vectors of  $A$ , where  $n^*$  is the number of these vectors, then  $V_S \overline{V_S}^T$  defines the projection onto the signal space of  $A$  and we consider  $P = I_n - V_S \overline{V_S}^T$ , where  $I_n$  is the  $n \times n$  identity matrix, with  $n > 3m$ . For any point  $z \in \Omega$ , let us define:  $W_c(z) := \frac{1}{\|Pg_{z,c}\|_2}$ , where the 2-norm  $\|\cdot\|_2$  is applied here to a vector of  $n$  components. The point  $z$  coincides with the location of an imperfection if and only if  $Pg_{z,c} = 0$ . In this way, we can form an image of detected imperfections by plotting  $W_c$  at each point  $z$  of  $\Omega$ ; the resulting plot will have large peaks at the locations of the imperfections.

The process is similar in the case where all the imperfections are electromagnetic. For  $1 \leq l, l' \leq n$  fixed, and replacing the approximation in (21) by the equality, the terms of the matrix  $A$  are in this case:

$$\begin{aligned} A_{ll'} &= \alpha^3 \sum_{j=1}^m \left[ k^2 \left( \frac{\varepsilon_0}{\varepsilon_j} - 1 \right) \left( M^j \left( \frac{\varepsilon_0}{\varepsilon_j} \right) \theta_l^\perp \right) \cdot \theta_{l'}^\perp \right. \\ &\quad \left. - k^2 \left( \frac{\mu_0}{\mu_j} - 1 \right) \left( M^j \left( \frac{\mu_0}{\mu_j} \right) (\theta_l \times \theta_l^\perp) \right) \cdot (\theta_{l'} \times \theta_{l'}^\perp) \right] e^{ik(\theta_l + \theta_{l'}) \cdot z_j}. \end{aligned}$$

Now,  $g_{z,c}$  is defined as follows:

$$g_{z,c} := \left( \left( \begin{array}{c} c \cdot \theta_1^\perp \\ c \cdot (\theta_1 \times \theta_1^\perp) \end{array} \right) e^{ik\theta_1 \cdot z}, \dots, \left( \begin{array}{c} c \cdot \theta_n^\perp \\ c \cdot (\theta_n \times \theta_n^\perp) \end{array} \right) e^{ik\theta_n \cdot z} \right)^T,$$

where  $c \in \mathbf{R}^3$  is some constant vector such that  $c \cdot \theta_l^\perp \neq 0$ , and  $c \cdot (\theta_l^\perp \times \theta_l) \neq 0$ , for all  $l = 1, \dots, n$ .

Referring again to [1], [2], if there exist  $5m$  significant singular-values of  $A$ , then there are  $m$  detectable imperfections, and if all the singular-values of  $A$  are zero or close to zero, then there are no detectable imperfections. An image of detected imperfections is also formed by plotting  $W_c(z) = \frac{1}{\|Pg_{z,c}\|_2}$  at each point  $z$  of  $\Omega$ , where  $P$  is built as previously from significant left singular-vectors of  $A$ ,  $n > 5m$  now, and the 2-norm  $\|\cdot\|_2$  is applied to an  $n \times 2$  matrix.

Hereafter, we present numerical results obtained from extensive simulations that make use of the procedure (cf. [6]) based on this approach. Since the visual representation of the functional  $W_c$  depending in particular on the parameter  $c$  is required, all our results will be described with respect to  $c$  in addition to the parameters  $\mu_\alpha$ ,  $\varepsilon_\alpha$  and  $\tau$  (see (20)). From the numerical inspection of the asymptotic formula (13) done in [6] as well as from other investigations of [6], the choices of  $\tau$  will be here such that  $\tau < 1$ . As the present procedure enforces an illumination of the domain  $\Omega$ , the results should be described also with respect to the number  $n$  of incident waves used to illuminate  $\Omega$ . These waves are defined from certain points uniformly distributed on the full boundary,  $\theta_l = (\cos(2\pi \frac{l-1}{n-1}) \sin(\pi \frac{l-1}{n-1}), \sin(2\pi \frac{l-1}{n-1}) \sin(\pi \frac{l-1}{n-1}), \cos(\pi \frac{l-1}{n-1}))^T$ ,  $1 \leq l \leq n$ . In a general way, we will consider  $n = 3m + 2$  incident waves in the case of electric

or magnetic imperfections, and  $n = 5m + 3$  in the case of the localization of electromagnetic imperfections. In our presentation of results, we will then specify the choice of  $n$  only when it differs from  $3m + 2$  or  $5m + 3$  following the case.

We fix here  $\mu_0 = \varepsilon_0 = 1$ . In order to compare the numerical results of the previous subsection with those that will be obtained here in the case of the localization of a single imperfection ( $m = 1$ ), we first consider most of the previous values of  $\tau$ ,  $\mu_1$  and  $\varepsilon_1$ , as well as  $\mathcal{T}_{h_1}$ ,  $\mathcal{T}_{h_2}$ . Let us recall that the same notation as above,  $p = (p_1, p_2, p_3)^T$ , is used to indicate the center of this imperfection.

Figures 13 - 16 present results obtained from the first level of the reduced mesh by considering  $\mu_1 = 1$ ,  $\varepsilon_1 = 3, 5$ ,  $\tau = 1.7 \cdot 10^{-2}, 2.6 \cdot 10^{-2}$  and  $c = (1.0, -2.0, 1.0)^T$ .

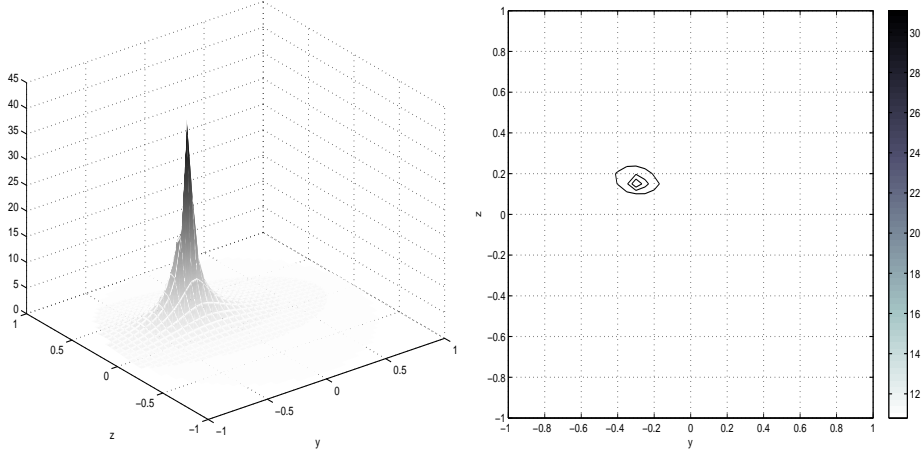


FIGURE 13. Cross-section of  $W_c$  at  $x = p_1$  (at left) and corresponding contour-plot (at right), from  $\mathcal{T}_{h_1}$  and with  $\mu_1 = 1$ ,  $\varepsilon_1 = 3$ ,  $\tau = 1.7 \cdot 10^{-2}$ ,  $c = (1.0, -2.0, 1.0)^T$ .

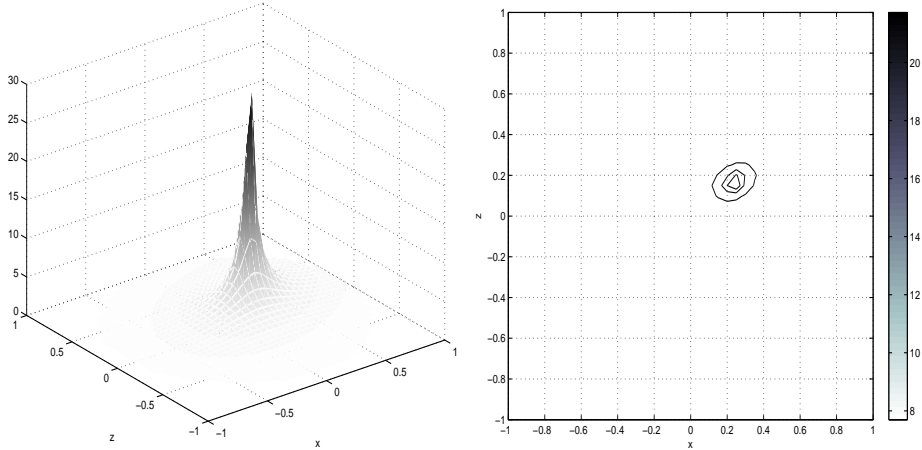


FIGURE 14. Cross-section of  $W_c$  at  $y = p_2$  (at left) and corresponding contour-plot (at right), from  $\mathcal{T}_{h_1}$  and with  $\mu_1 = 1$ ,  $\varepsilon_1 = 3$ ,  $\tau = 1.7 \cdot 10^{-2}$ ,  $c = (1.0, -2.0, 1.0)^T$ .

These results concerning the location of the single imperfection seem more accurate

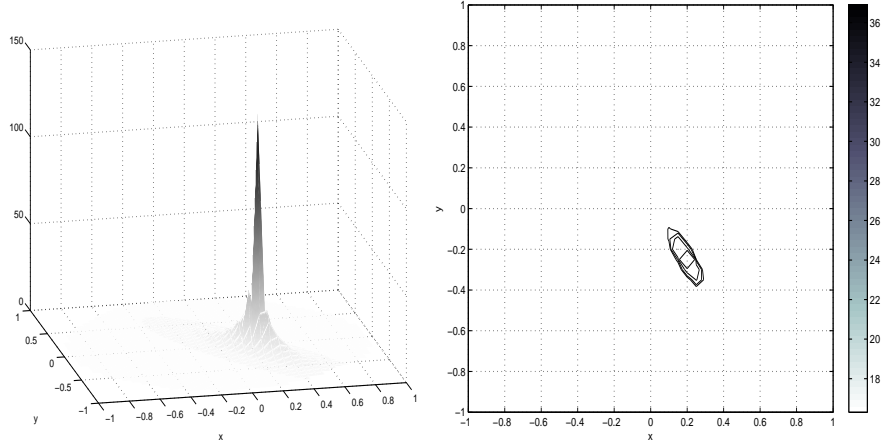


FIGURE 15. Cross-section of  $W_c$  at  $z = p_3$  (at left) and corresponding contour-plot (at right), from  $\mathcal{T}_{h_1}$  and with  $\mu_1 = 1$ ,  $\varepsilon_1 = 3$ ,  $\tau = 1.7 \cdot 10^{-2}$ ,  $c = (1.0, -2.0, 1.0)^T$ .

than those of Figures 6 and 7 obtained in the previous subsection.

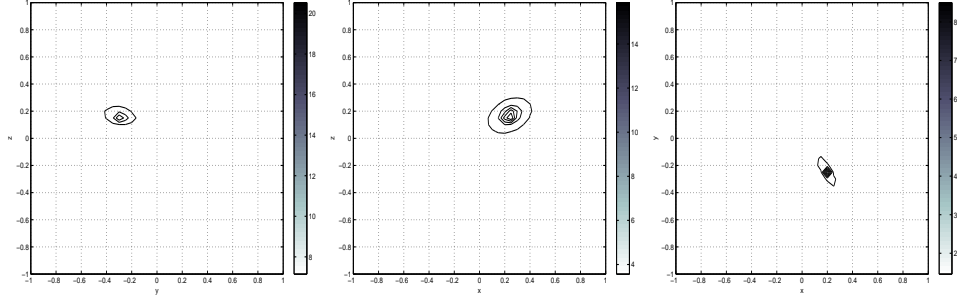


FIGURE 16. Respective contour-plots of cross-sections of  $W_c$  at  $x = p_1$ ,  $y = p_2$  and  $z = p_3$ , from  $\mathcal{T}_{h_1}$  and with  $\mu_1 = 1$ ,  $\varepsilon_1 = 5$ ,  $\tau = 2.6 \cdot 10^{-2}$ ,  $c = (1.0, -2.0, 1.0)^T$ .

By using now the second level of the reduced mesh in the latter case ( $\mu_1 = 1$  with  $\varepsilon_1 = 5$ ), we obtain the results of Figure 17.

Though slightly less accurate, these results are similar to those of Figure 16 obtained at the same frequency and with the same value of the parameter  $c$ . Similar conclusions are also reached when we compare the results of Figures 13 - 15 with those obtained with the same values of parameters but from  $\mathcal{T}_{h_2}$ . From this point on, we treat only experiments based on  $\mathcal{T}_{h_2}$ , due to the efficiency in CPU time for simulations with this second level of the reduced mesh and the fact that the difference of the localization results, between  $\mathcal{T}_{h_1}$  and  $\mathcal{T}_{h_2}$ , is not numerically very significant.

Let us also mention in a general way that the choice of values of  $c$  will always be done as described at the beginning of this subsection and that other admissible values for this parameter led to the same kind of results as here.

As already observed in Figure 12, when the procedure based on the Current Projection was used, the results of Figure 18 indicate, in the case of the present

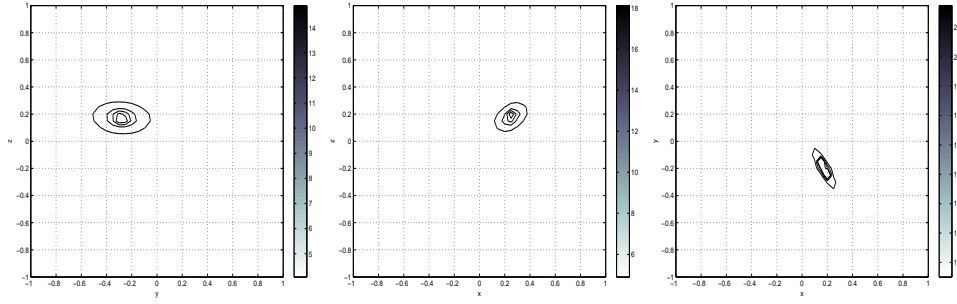


FIGURE 17. Respective contour-plots of cross-sections of  $W_c$  at  $x = p_1$ ,  $y = p_2$  and  $z = p_3$ , from  $\mathcal{T}_{h_2}$  and with  $\mu_1 = 1$ ,  $\varepsilon_1 = 5$ ,  $\tau = 2.6 \cdot 10^{-2}$ ,  $c = (1.0, -2.0, 1.0)^T$ .

procedure, that the location of the imperfection becomes less accurate when smaller frequencies are considered.

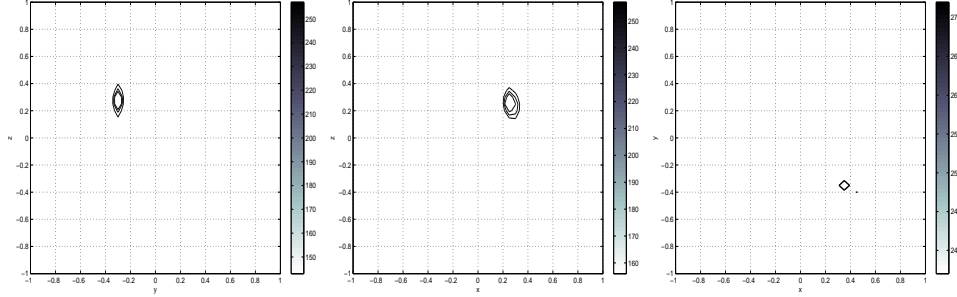


FIGURE 18. Respective contour-plots of cross-sections of  $W_c$  at  $x = p_1$ ,  $y = p_2$  and  $z = p_3$ , from  $\mathcal{T}_{h_2}$  and with  $\mu_1 = 10$ ,  $\varepsilon_1 = 1$ ,  $\tau = 8.2 \cdot 10^{-3}$ ,  $c = (-1.0, 1.0, 1.0)^T$ .

Contrary to the localization procedure of the previous subsection, where a restriction was enforced on the choice of frequencies for reconstructions, the present procedure allows us to achieve localizations in a less restrictive context, namely with 'high' frequencies. The results obtained by considering larger values of  $\tau$  are represented in Figures 19 - 20, for weak and strong contrasts.

Contrary also to the previous subsection, we can achieve here simulations of the localization of an electromagnetic imperfection. Figures 21 - 22 show results of such a localization obtained at different frequencies.

Let us mention that independently of the contrast of the domain, the localization of the center of the imperfection becomes less and less accurate when  $\tau$  takes larger values. With  $\tau \geq 3.5 \cdot 10^{-1}$  for example, we obtain disastrous results from the simulations.

We now treat the localization of multiple imperfections from the settings based on  $\mathcal{T}_h^4$  and  $\mathcal{T}_h^5$ . The presentation of our results will consist here of showing contour-plot views of the functional  $W_c$  from each one of the three coordinate directions. In this postprocessing, when the  $z$ -direction, for example, will be concerned, the used software will draw, besides contour-plot obtained on the plane  $Oxy$ , horizontal and vertical segments whose intersections correspond to centers of the original imperfections viewed on  $Oxy$ .

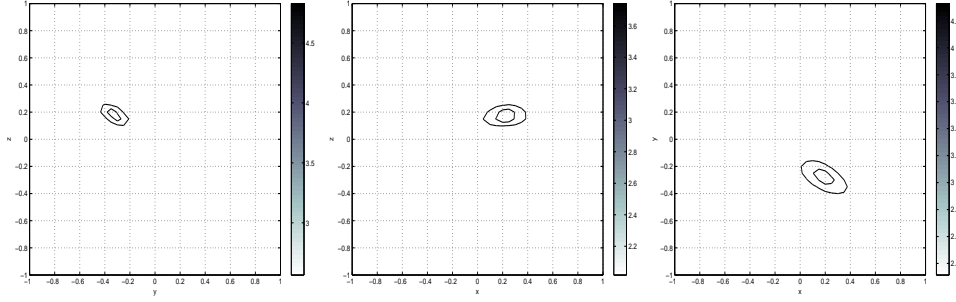


FIGURE 19. Respective contour-plots of cross-sections of  $W_c$  at  $x = p_1$ ,  $y = p_2$  and  $z = p_3$ , from  $\mathcal{T}_{h_2}$  and with  $\mu_1 = 1$ ,  $\varepsilon_1 = 3$ ,  $\tau = 6.6 \cdot 10^{-2}$ ,  $c = (1.0, -2.0, 1.0)^T$ .

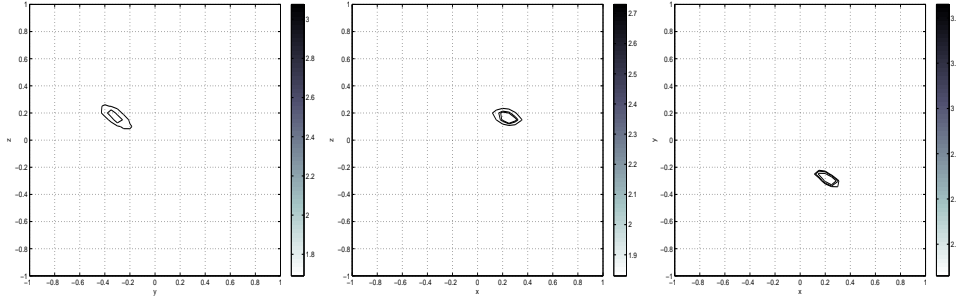


FIGURE 20. Respective contour-plots of cross-sections of  $W_c$  at  $x = p_1$ ,  $y = p_2$  and  $z = p_3$ , from  $\mathcal{T}_{h_2}$  and with  $\mu_1 = 1$ ,  $\varepsilon_1 = 10$ ,  $\tau = 1.06 \cdot 10^{-1}$ ,  $c = (1.0, -2.0, 1.0)^T$ .

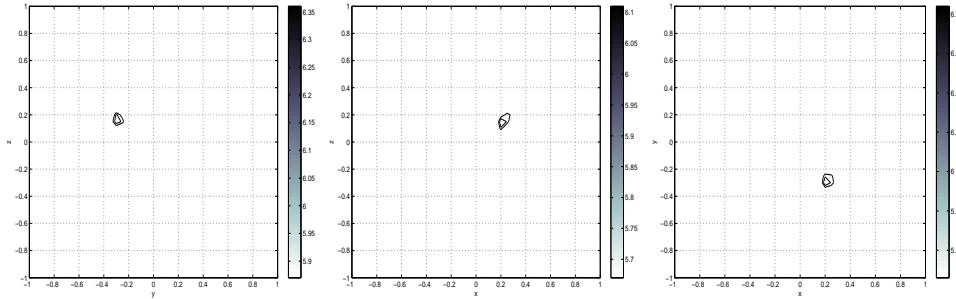


FIGURE 21. Respective contour-plots of cross-sections of  $W_c$  at  $x = p_1$ ,  $y = p_2$  and  $z = p_3$ , from  $\mathcal{T}_{h_2}$  and with  $\mu_1 = 5$ ,  $\varepsilon_1 = 10$ ,  $\tau = 1.06 \cdot 10^{-1}$ ,  $c = (-1.0, -0.5, 0.5)^T$ .

The results represented in Figures 23 - 25 are obtained at a same frequency but with different contrasts of the domain.

Figure 26 presents the results obtained by keeping the same values of  $\mu_\alpha$ ,  $\varepsilon_\alpha$  as in Figure 23 and the same frequency, but by considering  $\mathcal{T}_h^5$  with a larger number of incident waves.

We can already summarize this subsection by reporting that the localization of the imperfections from the procedure based on the MUSIC approach is efficiently

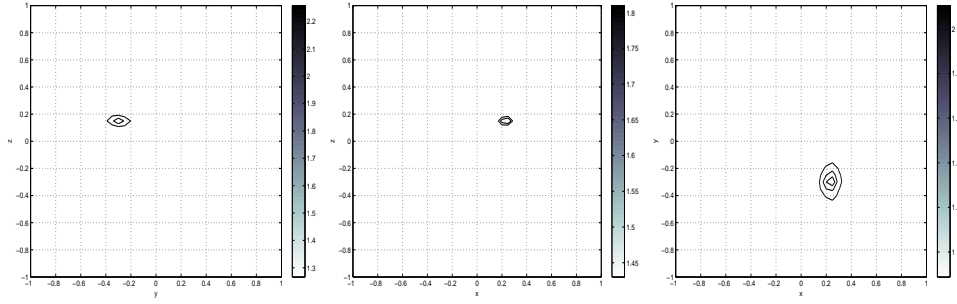


FIGURE 22. Respective contour-plots of cross-sections of  $W_c$  at  $x = p_1$ ,  $y = p_2$  and  $z = p_3$ , from  $\mathcal{T}_{h_2}$  and with  $\mu_1 = 5$ ,  $\varepsilon_1 = 10$ ,  $\tau = 2.26 \cdot 10^{-1}$ ,  $c = (-0.5, 2, -0.5)^T$ .

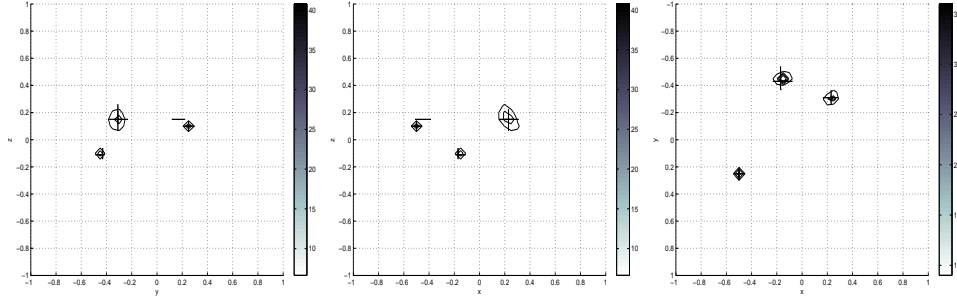


FIGURE 23. Contour-plot views of  $W_c$  from the  $x$ -direction, the  $y$ -direction and the  $z$ -direction respectively, when  $\mathcal{T}_h^4$  is used,  $\mu_j = 1$ ,  $\varepsilon_j = 3$  ( $1 \leq j \leq 3$ ),  $\tau = 1.007 \cdot 10^{-1}$  and  $c = (1.5, -0.5, 2.5)^T$ .

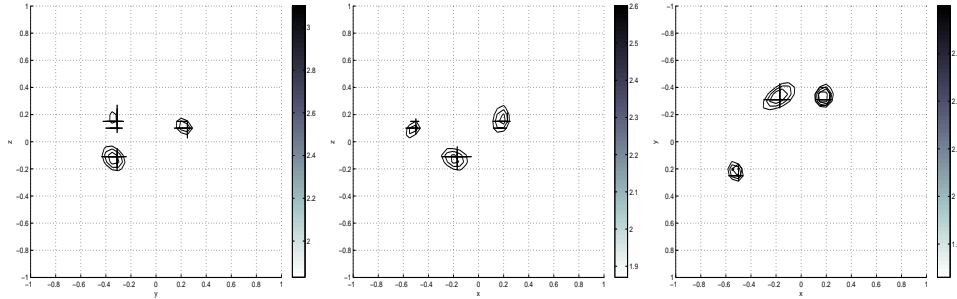


FIGURE 24. Contour-plot views of  $W_c$  from the  $x$ -direction, the  $y$ -direction and the  $z$ -direction respectively, when  $\mathcal{T}_h^4$  is used,  $\mu_j = 5$ ,  $\varepsilon_j = 3$  ( $1 \leq j \leq 3$ ),  $\tau = 1.007 \cdot 10^{-1}$  and  $c = (2.0, -2.5, 1.5)^T$ .

achieved as long as too small or large values of  $\tau$  are not considered. As was observed in [6], where full meshes were used, it appears here that the accuracy of the localization of the imperfections varies also with respect to the contrast of the domain. The results seem slightly more accurate in the case of electric imperfections than in other cases, independently of the considered reduced meshes.

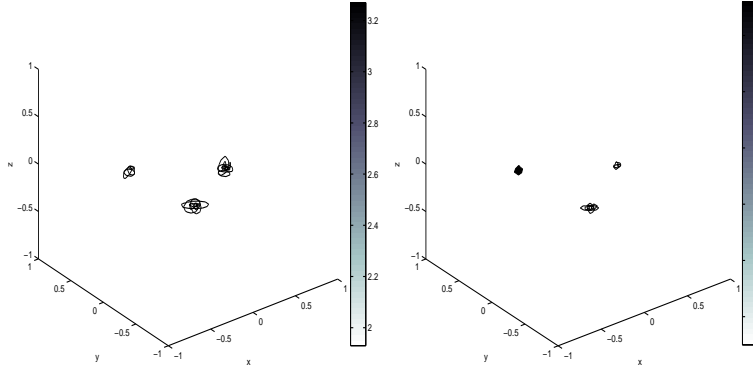


FIGURE 25. Contour-plot views of  $W_c$  when  $\mathcal{T}_h^4$  is used,  $\tau = 1.00710^{-1}$ ,  $c = (2.0, -2.5, 1.5)^T$ , with  $\mu_j = 5$ ,  $\varepsilon_1 = \varepsilon_2 = 3$ ,  $\varepsilon_3 = 3 + 0.1i$  at left, and  $\mu_j = 3$ ,  $\varepsilon_j = 10$  at right,  $1 \leq j \leq 3$ .

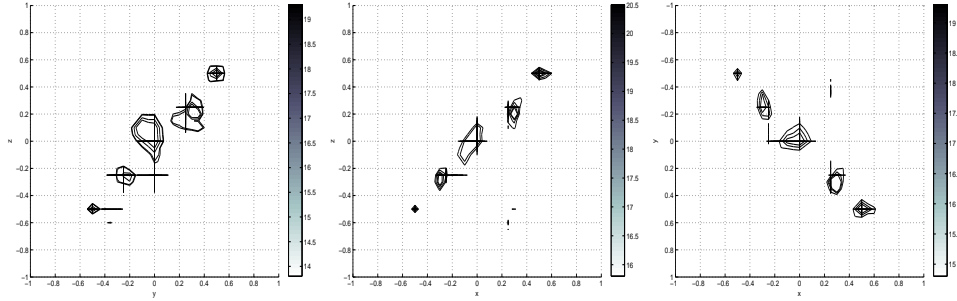


FIGURE 26. Contour-plot views of  $W_c$  from the  $x$ -direction, the  $y$ -direction and the  $z$ -direction respectively, when  $\mathcal{T}_h^5$  is used,  $\mu_j = 1$ ,  $\varepsilon_j = 3$  ( $1 \leq j \leq 5$ ),  $\tau = 1.06 \cdot 10^{-1}$ ,  $c = (1.0, 2.5, 1.0)^T$  and  $n = 30$ .

**5.4. From a Procedure based on an Inverse Fourier Method.** In this last subsection, we describe the numerical results obtained from, also, a procedure aimed both at localizing a single imperfection as well as multiple imperfections. As presented in [6], this procedure makes use of the asymptotic formula (15) and of the original idea of Calderón [8] which was to reduce the localization problem to the calculation of an inverse Fourier transform. Let us first of all recall briefly the principle of this procedure by reconsidering the formula (15) as follows:

$$\begin{aligned}
 \Gamma &:= \int_{\partial\Omega} \operatorname{curl} E_\alpha \times \nu \cdot w \, d\sigma - \int_{\partial\Omega} \operatorname{curl} w \times \nu \cdot (\nu \times g) \, d\sigma = \\
 (22) \quad &\alpha^3 \sum_{j=1}^m k^2 \left( \frac{\varepsilon_0}{\varepsilon_j} - 1 \right) \left[ M^j \left( \frac{\varepsilon_0}{\varepsilon_j} \right) E_0(z_j) \right] \cdot w(z_j) + \\
 &\alpha^3 \sum_{j=1}^m \left( \frac{\mu_0}{\mu_j} - 1 \right) \left[ M^j \left( \frac{\mu_0}{\mu_j} \right) \operatorname{curl} E_0(z_j) \right] \cdot \operatorname{curl} w(z_j) + O(\alpha^4),
 \end{aligned}$$

where  $g = E_\alpha \times \nu$ .

For an arbitrary  $\eta \in \mathbb{R}^3$ , let us define  $\beta$  and  $\zeta$  in  $\mathbb{R}^3$  such that:

$$\begin{cases} \|\beta\|^2 = 1, & \beta \cdot \eta = 0, \\ \|\zeta\|^2 = 1, & \zeta \cdot \eta = \zeta \cdot \beta = 0, \end{cases}$$

with  $\|\cdot\|$  denoting the usual norm associated with the Hermitian product on  $\mathbb{C}^3$ . Let  $p = \eta + \gamma\beta$  such that  $p \cdot p = k^2$ , i.e.,  $\gamma$  is a complex number such that:  $\gamma^2 = k^2 - \|\eta\|^2$ . In accordance with (14), we consider  $w(x) = e^{iq \cdot x} \zeta$  as the test vector field, where  $q = \eta - \gamma\beta$ . By taking  $g(x) = (e^{ip \cdot x} \zeta) \times \nu(x)$  as the boundary current, then associated with the background potential  $E_0(x) = e^{ip \cdot x} \zeta$ , it follows from (22) that:

$$(23) \quad \begin{aligned} \Gamma &= \alpha^3 \sum_{j=1}^m \left( k^2 \left( \frac{\varepsilon_0}{\varepsilon_j} - 1 \right) \left[ M^j \left( \frac{\varepsilon_0}{\varepsilon_j} \right) e^{ip \cdot z_j} \zeta \right] \cdot e^{iq \cdot z_j} \zeta + \right. \\ &\quad \left. \left( \frac{\mu_0}{\mu_j} - 1 \right) \left[ M^j \left( \frac{\mu_0}{\mu_j} \right) (ie^{ip \cdot z_j} p \times \zeta) \right] \cdot (ie^{iq \cdot z_j} q \times \zeta) \right) + O(\alpha^4). \end{aligned}$$

By viewing the measurement as a function of  $\eta$  now,

$$\begin{aligned} \Gamma(\eta) &\approx \alpha^3 \sum_{j=1}^m \left( k^2 \left( \frac{\varepsilon_0}{\varepsilon_j} - 1 \right) \left[ M^j \left( \frac{\varepsilon_0}{\varepsilon_j} \right) \zeta \right] \cdot \zeta - \right. \\ &\quad \left. \left( \frac{\mu_0}{\mu_j} - 1 \right) \left[ M^j \left( \frac{\mu_0}{\mu_j} \right) ((\eta + \gamma\beta) \times \zeta) \right] \cdot ((\eta - \gamma\beta) \times \zeta) \right) e^{i2\eta \cdot z_j}, \end{aligned}$$

and by inspecting the context where all the imperfections are balls — the tensors  $M^j(c)$  being accordingly of the form  $m^j(c)I_3$  with  $m^j(c)$  a scalar depending on  $c$  (cf. e.g. [6]), it follows that

$$(24) \quad \Gamma(\eta) \approx \alpha^3 \sum_{j=1}^m \left[ k^2 \left( \frac{\varepsilon_0}{\varepsilon_j} - 1 \right) m^j \left( \frac{\varepsilon_0}{\varepsilon_j} \right) - \left( \frac{\mu_0}{\mu_j} - 1 \right) m^j \left( \frac{\mu_0}{\mu_j} \right) (2\|\eta\|^2 - k^2) \right] e^{i2\eta \cdot z_j}.$$

Since  $\|\eta\|^2$  is a polynomial in the coordinates  $\eta_i$ ,  $1 \leq i \leq 3$ , of  $\eta$ , the expression in the right-hand side of (24) is therefore, in this particular case, the Fourier transform of a linear combination of derivatives of order less than or equal to 2 of delta functions centered at the points  $-2z_j$ ,  $1 \leq j \leq m$ . More precisely, the inverse Fourier transform of  $\Gamma(\eta)$  is expressed as:

$$\check{\Gamma}(x) \approx \alpha^3 \sum_{j=1}^m L_j(\delta_{-2z_j})(x),$$

where  $L_j$  is a second order differential operator with constant coefficients depending on  $m^j(\frac{\varepsilon_0}{\varepsilon_j})$  and  $m^j(\frac{\mu_0}{\mu_j})$ . In this approach, a numerical Fourier inversion of a sample of measurements should efficiently pin down the  $z_j$ 's.

When some of the imperfections are not balls, we may rewrite (23) as below, where the measurement  $\Gamma$  is viewed again as a function of  $\eta$ :

$$(25) \quad \Gamma(\eta) \approx \alpha^3 \sum_{j=1}^m \left( k^2 \left( \frac{\varepsilon_0}{\varepsilon_j} - 1 \right) T_{\varepsilon_0, \varepsilon_j}(\eta) - \left( \frac{\mu_0}{\mu_j} - 1 \right) T_{\mu_0, \mu_j}(\eta) \right) e^{i2\eta \cdot z_j},$$

with  $T_{\varepsilon_0, \varepsilon_j}(\eta) = (M^j(\frac{\varepsilon_0}{\varepsilon_j}) \zeta) \cdot \zeta$  and  $T_{\mu_0, \mu_j}(\eta) = (M^j(\frac{\mu_0}{\mu_j})((\eta + \gamma\beta) \times \zeta)) \cdot ((\eta - \gamma\beta) \times \zeta)$ . The expression in the right-hand side of (25) is in fact the Fourier transform of an operator of a more complicated kind acting on delta functions centered at the points  $-2z_j$ ,  $1 \leq j \leq m$ . The present localization principle consists of sampling  $\Gamma(\eta)$  at some discrete set of points and then evaluating the discrete inverse Fourier

transform of the corresponding sample. After a rescaling (by  $-\frac{1}{2}$ ), the support of this inverse Fourier transform will provide the locations of the imperfections.

Typically, for each point  $\eta$  (of the mentioned discrete set), we consider  $g(x) = (e^{i(\eta+\gamma\beta)\cdot x}\zeta) \times \nu(x)$  as the boundary current in (7) and compute through (16) the corresponding discrete electric field, denoted here by  $E_\alpha^h$ . After determining the discrete field,  $\text{curl}E_\alpha^h \times \nu$ , we evaluate numerically the measurement  $\Gamma(\eta)$  by using of course  $w(x) = e^{i(\eta-\gamma\beta)\cdot x}\zeta$  as the test field in  $\int_{\partial\Omega} \text{curl} E_\alpha \times \nu \cdot w \, d\sigma - \int_{\partial\Omega} \text{curl} w \times \nu \cdot (\nu \times g) \, d\sigma$ , and by replacing  $E_\alpha$  by  $E_\alpha^h$  in this difference of terms.

Let us now specify, following [22], a possible way to choose a step size for sampling with respect to  $\eta$  in the numerical simulations. First of all, let us assume that all the centers  $z_j = (z_j^1, z_j^2, z_j^3)^T$  of the imperfections ( $1 \leq j \leq m$ ) lie in a domain  $[-K, K]^3$ , where the bound  $K$  is known. To simplify the presentation, let us consider the formula (24) and rewrite simply its right-hand side as:

$$(26) \quad \sum_{j=1}^m C_j e^{2i(\eta_1 z_j^1 + \eta_2 z_j^2 + \eta_3 z_j^3)},$$

where the complex constants  $C_j$  are unknown. As previously mentioned, for each  $\eta = (\eta_1, \eta_2, \eta_3)^T$ , we are able to evaluate the measurement  $\Gamma(\eta)$  and therefore we assume that (26) is known for  $(\eta_1, \eta_2, \eta_3)^T \in [-\eta_{\max}, \eta_{\max}]^3$ , on a regular grid made up of  $n^3$  points. We are then in possession of the sequence of data:

$$\sum_{j=1}^m C_j e^{2i((-\eta_{\max}+(l_1-1)\rho)z_j^1 + (-\eta_{\max}+(l_2-1)\rho)z_j^2 + (-\eta_{\max}+(l_3-1)\rho)z_j^3)}, \quad 1 \leq l_1, l_2, l_3 \leq n,$$

where  $\rho = \frac{2\eta_{\max}}{n}$ . After applying the inverse Fourier transform to this sequence, we get

$$(27) \quad \frac{1}{n^3} \sum_{j=1}^m C_j \sum_{1 \leq l_1, l_2, l_3 \leq n} e^{2i((-\eta_{\max}+(l_1-1)\rho)z_j^1 + (-\eta_{\max}+(l_2-1)\rho)z_j^2 + (-\eta_{\max}+(l_3-1)\rho)z_j^3)} \\ \times e^{2i\pi(\frac{(l_1-1)}{n}(s_1-1) + \frac{(l_2-1)}{n}(s_2-1) + \frac{(l_3-1)}{n}(s_3-1))},$$

with  $1 \leq s_1, s_2, s_3 \leq n$ . Let us now consider the module of the term in (27), reduced as follows:

$$(28) \quad \left| \sum_{j=1}^m \frac{1}{n^3} 8C_j \frac{\sin(2\eta_{\max}z_j^1) \sin(2\eta_{\max}z_j^2) \sin(2\eta_{\max}z_j^3)}{(e^{2\pi(\frac{\rho z_j^1}{\pi} + \frac{s_1-1}{n})i} - 1)(e^{2\pi(\frac{\rho z_j^2}{\pi} + \frac{s_2-1}{n})i} - 1)(e^{2\pi(\frac{\rho z_j^3}{\pi} + \frac{s_3-1}{n})i} - 1)} \right|.$$

Then, as  $n$  becomes large, the quantity in (28) is small unless one of the terms  $\frac{\rho z_j^1}{\pi} + \frac{s_1-1}{n}$ ,  $\frac{\rho z_j^2}{\pi} + \frac{s_2-1}{n}$ , and  $\frac{\rho z_j^3}{\pi} + \frac{s_3-1}{n}$  is close to an integer. By enforcing (for example)  $\frac{K\rho}{\pi} \lesssim \frac{1}{3}$ , each one of the previous terms shall only approach the integers 0 or 1, in the case where  $n$  becomes large ( $n \geq 3$ ). This relation provides a practical way to choose the step size  $\rho$  and also indicates a link between  $\eta_{\max}$ ,  $K$  and  $n$ . In fact, we have  $\rho = \frac{2\eta_{\max}}{n}$  and take

$$(29) \quad \rho \approx \frac{1}{K}.$$

We shall fix  $\rho$  according to (29) and consider simultaneously increasing values of  $n$  and of  $\eta_{\max}$  for more accuracy. This is a resolution method whose centers  $z_j$ ,

$1 \leq j \leq m$ , are localized from the sequence of the modules of the terms in (27), with at best (theoretically) a resolution of order  $\frac{\pi}{2\eta_{\max}}$ .

As presented in [6], the procedure based on this approach incorporates additionally a cutoff process aimed at overcoming numerical instabilities that could occur in the presence of a large disproportion between the magnitude of the remainder term of (23) for large values of  $\|\eta\|$ , and the magnitude of the right-hand side of (25), or then the magnitude of (26), for  $\|\eta\|$  near 0. In this cutoff process, initially summarized in a two-dimensional situation by D. Volkov in [22], a threshold  $\eta_*$  (independent of the centers and shapes of imperfections as well as of  $\mu_\alpha, \varepsilon_\alpha$ ) is introduced such that for  $\|\eta\| > \|(\eta_*, \eta_*, \eta_*)^T\|$ , the quantity in (26) is set equal to 0. Consequently, “fine” grids for  $\eta$  are recommended, in order to “compensate” the induced loss of accuracy.

The presentation of our results will consist here of representing, after a rescaling by  $-\frac{1}{2}$ , contour-plots based on the sequence of modules of the terms that approximate those of (27), following the asymptotic formula for measurements, furthermore enriched by a usual linear interpolation process. In addition to the physical parameters  $\mu_\alpha, \varepsilon_\alpha$  and  $\tau$ , all our results will be then described with respect to  $\eta_{\max}$ ,  $n$  and  $\eta_*$ . Of course, as in the previous localization approaches, each experiment considered here will make use of computations in double precision.

We want to compare the numerical results of Subsections 5.2 and 5.3 with those that will be described below in the case of the localization of a single imperfection ( $m = 1$ ) and on the other hand, to compare the results of Subsection 5.3 with those that will be obtained here in the case of the localization of multiple imperfections ( $m > 1$ ). In all the cases we fix  $\mu_0 = \varepsilon_0 = 1$  and the choices of  $\eta_*$  will result from numerical tests. The choices of the parameter  $\tau$  will be such that  $\tau < 1$ , motivated as in the previous subsection.

Figures 27 - 33 present the results of the localization of a single imperfection, in each one of the settings defined from  $\mathcal{T}_{h_1}$  and  $\mathcal{T}_{h_2}$ ; most of the values of  $\mu_1, \varepsilon_1, \tau$  considered in Subsections 5.2 and 5.3 are used here. An order of resolution  $\frac{\pi}{2\eta_{\max}} \approx 0.157$  is expected for each experiment, since we fix  $\eta_{\max} = 10$  and consider  $\rho = 2$  as the step size for sampling, i.e.  $n = 10$ .

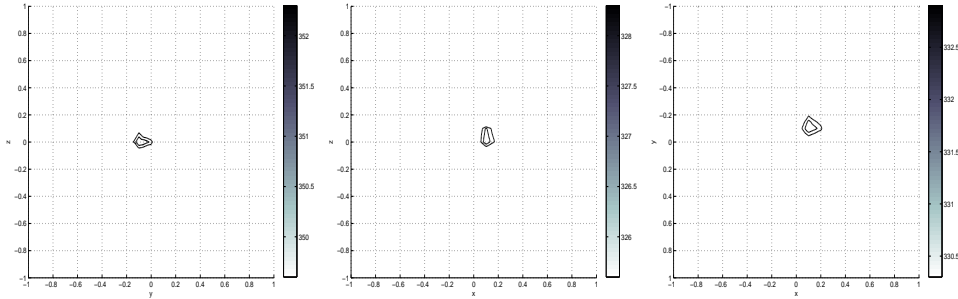


FIGURE 27. Contour-plot views respectively from the  $x$ -direction, the  $y$ -direction and the  $z$ -direction, based on the enriched sequence, deriving from one of the modules of the terms that approximate those of (27). Here,  $\mathcal{T}_{h_1}$  is used,  $\mu_1 = 1, \varepsilon_1 = 3, \tau = 1.7 \cdot 10^{-2}, \eta_{\max} = 10, n = 10$  and  $\eta_* = 10$ .

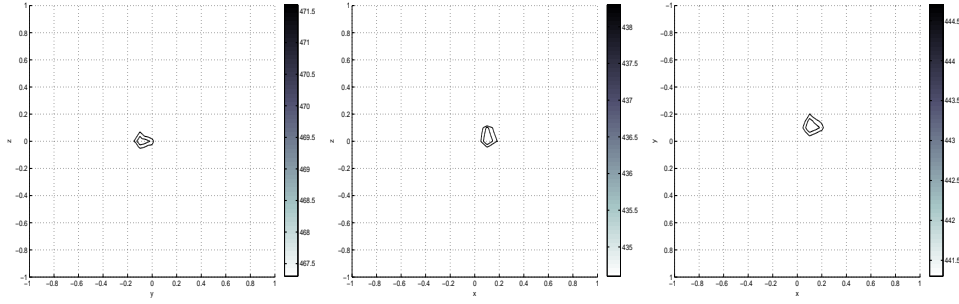


FIGURE 28. Contour-plot views respectively from the  $x$ -direction, the  $y$ -direction and the  $z$ -direction, based on the enriched sequence, deriving from one of the modules of the terms that approximate those of (27). Here,  $\mathcal{T}_{h_1}$  is used,  $\mu_1 = 1$ ,  $\varepsilon_1 = 5$ ,  $\tau = 2.6 \cdot 10^{-2}$ ,  $\eta_{\max} = 10$ ,  $n = 10$  and  $\eta_\star = 10$ .

The results of Figures 27 - 28 are accurate according to the expected order of resolution. However, these results are less accurate when compared with those of Figures 6 - 7 that derive from the procedure based on the Current Projection method. As opposed to that procedure, we can here perform simulations with 'higher' frequencies.

Figure 29 presents the results of the localization (of a same type of imperfection as previously) obtained also from the first level of the reduced mesh, but at a higher frequency.

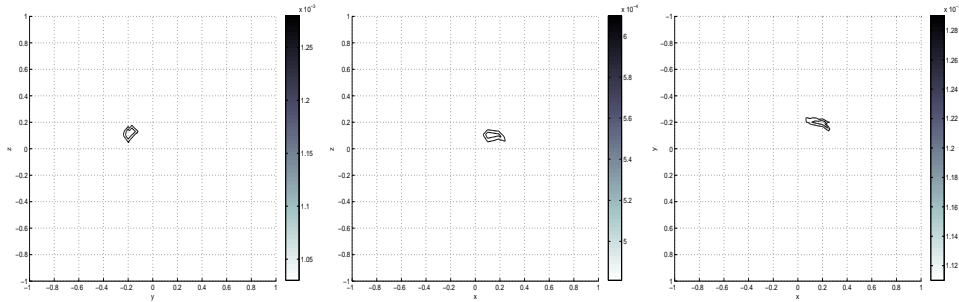


FIGURE 29. Contour-plot views respectively from the  $x$ -direction, the  $y$ -direction and the  $z$ -direction, based on the enriched sequence, deriving from one of the modules of the terms that approximate those of (27). Here,  $\mathcal{T}_{h_1}$  is used,  $\mu_1 = 1$ ,  $\varepsilon_1 = 10$ ,  $\tau = 1.06 \cdot 10^{-1}$ ,  $\eta_{\max} = 10$ ,  $n = 10$  and  $\eta_\star = 5$ .

The results of Figure 30, that derive from the second level of the reduced mesh, are similar to those of Figure 29 obtained with the same values of  $\mu_1$ ,  $\varepsilon_1$ ,  $\eta_{\max}$ ,  $n$ , and at the same frequency.

Similar comparisons of experiments between these reduced mesh levels allow us to notice the efficiency of the localization with the second level of the reduced mesh with respect to the CPU time, though, apparently, slightly less accurate than the localization from the first level of the reduced mesh. We are thus concerned with  $\mathcal{T}_{h_2}$  in the experiments providing the results presented below in Figures 31 - 33. As

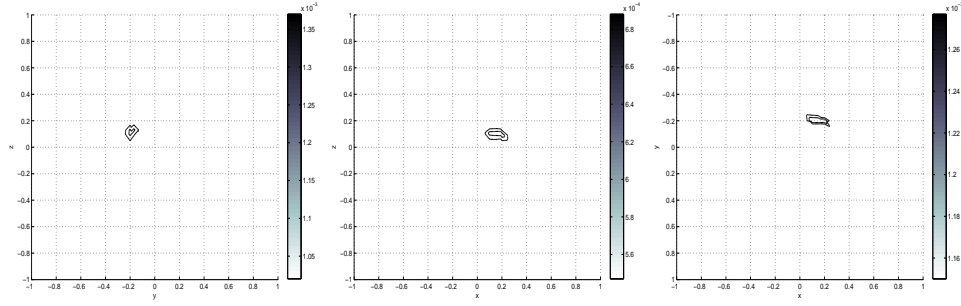


FIGURE 30. Contour-plot views respectively from the  $x$ -direction, the  $y$ -direction and the  $z$ -direction, based on the enriched sequence, deriving from one of the modules of the terms that approximate those of (27). Here,  $\mathcal{T}_{h_2}$  is used,  $\mu_1 = 1$ ,  $\varepsilon_1 = 10$ ,  $\tau = 1.06 \cdot 10^{-1}$ ,  $\eta_{\max} = 10$ ,  $n = 10$  and  $\eta_* = 5$ .

with the procedure of the previous subsection, we can localize an electromagnetic imperfection with the present approach.

The results of Figure 31 are less accurate than those of Figure 22 represented in the previous subsection. In fact, from similar experiments, the results obtained from the present approach, and with the considered value of  $\eta_{\max}$ , are less accurate than those provided from the MUSIC approach. However, the accuracy of the present approach could be improved by increasing the value of  $\eta_{\max}$ .

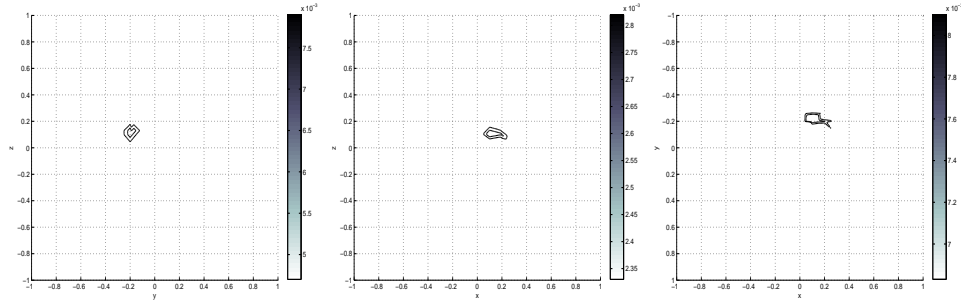


FIGURE 31. Contour-plot views respectively from the  $x$ -direction, the  $y$ -direction and the  $z$ -direction, based on the enriched sequence, deriving from one of the modules of the terms that approximate those of (27). Here,  $\mathcal{T}_{h_2}$  is used,  $\mu_1 = 5$ ,  $\varepsilon_1 = 10$ ,  $\tau = 2.26 \cdot 10^{-1}$ ,  $\eta_{\max} = 10$ ,  $n = 10$  and  $\eta_* = 6$ .

Figures 32 - 33 present the localization of a single imperfection achieved at a higher frequency and for different contrasts.

The localization of the imperfection is again successfully achieved, but we obtain disastrous results from the simulations when larger values of the frequency are used.

Let us now inspect the localization context of multiple imperfections, in various aspects. For this inspection, we fix  $\rho = \frac{5}{4}$  and are led to use a bigger number of measurements than previously. The presentation of our results will consist again of showing, from each one of the three coordinate directions, and after a rescaling by  $-\frac{1}{2}$ , contour-plot views based on the sequence (enriched by a linear interpolation

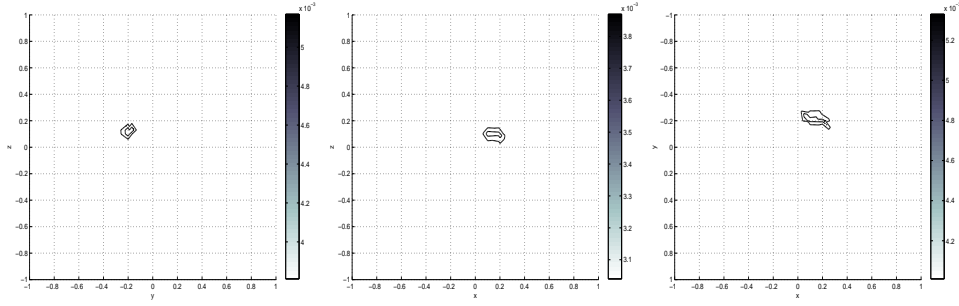


FIGURE 32. Contour-plot views respectively from the  $x$ -direction, the  $y$ -direction and the  $z$ -direction, based on the enriched sequence, deriving from one of the modules of the terms that approximate those of (27). Here,  $\mathcal{T}_{h_2}$  is used,  $\mu_1 = 1$ ,  $\varepsilon_1 = 3$ ,  $\tau = 3.46 \cdot 10^{-1}$ ,  $\eta_{\max} = 10$ ,  $n = 10$  and  $\eta_* = 6$ .

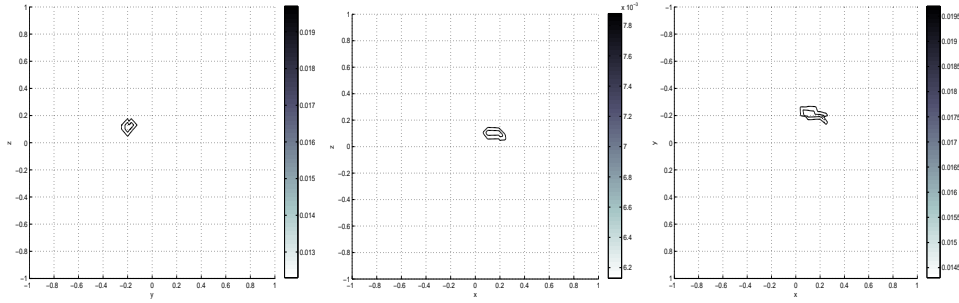


FIGURE 33. Contour-plot views respectively from the  $x$ -direction, the  $y$ -direction and the  $z$ -direction, based on the enriched sequence, deriving from one of the modules of the terms that approximate those of (27). Here,  $\mathcal{T}_{h_2}$  is used,  $\mu_1 = 5$ ,  $\varepsilon_1 = 10$ ,  $\tau = 3.46 \cdot 10^{-1}$ ,  $\eta_{\max} = 10$ ,  $n = 10$  and  $\eta_* = 6$ .

process) deriving from one of the modules of the terms that approximate those of (27). Also as in the previous subsection, when the  $z$ -direction, for example, will be concerned, the software used for the present postprocessing will draw, besides contour-plot obtained on the plane  $Oxy$ , horizontal and vertical segments whose intersections correspond to centers of the original imperfections viewed on  $Oxy$ .

We first consider experiments regarding the configuration based on  $\mathcal{T}_h^4$ .

Figures 34 - 35 present the results of the localization of three imperfections achieved at different frequencies. In comparison with the results of Figure 25, obtained from the MUSIC approach, those of Figure 34 are less accurate.

The experiments associated with Figures 36 - 37 use the same frequency as in the localization corresponding to Figure 35, but consider stronger contrasts.

This localization based on  $\mathcal{T}_h^4$  is also successfully obtained, in the limit of the resolution.

In what follows, we consider experiments regarding the configuration based on  $\mathcal{T}_h^5$ . Figure 38 presents the results of the localization of five electric imperfections

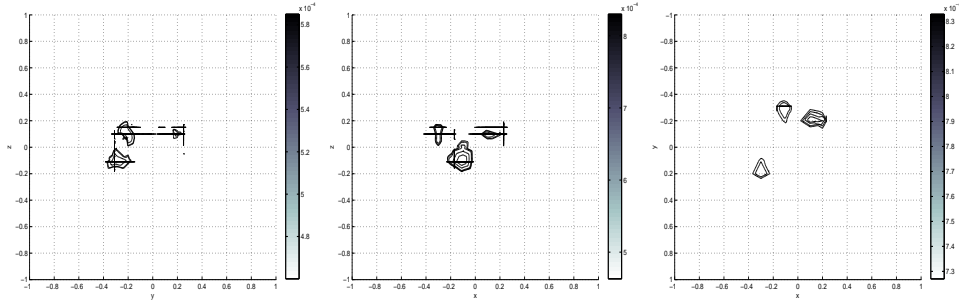


FIGURE 34. Contour-plot views respectively from the  $x$ -direction, the  $y$ -direction and the  $z$ -direction, based on the enriched sequence, deriving from one of the modules of the terms that approximate those of (27). Here,  $\mathcal{T}_h^4$  is used,  $\mu_j = 3$ ,  $\varepsilon_j = 10$  ( $1 \leq j \leq 3$ ),  $\tau = 1.007 10^{-1}$ ,  $\eta_{\max} = 10$ ,  $n = 16$  and  $\eta_\star = 5$ .

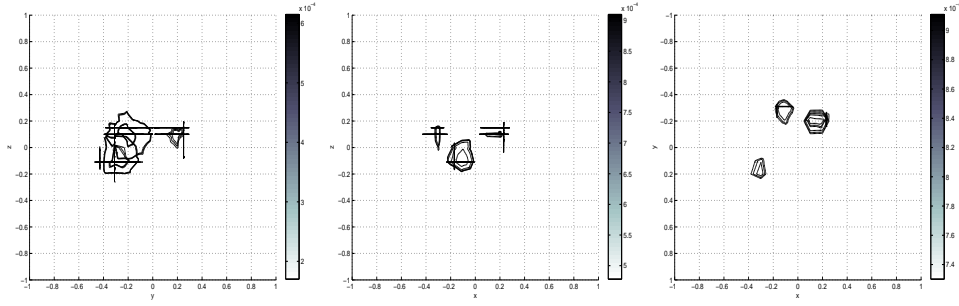


FIGURE 35. Contour-plot views respectively from the  $x$ -direction, the  $y$ -direction and the  $z$ -direction, based on the enriched sequence, deriving from one of the modules of the terms that approximate those of (27). Here,  $\mathcal{T}_h^4$  is used,  $\mu_j = 1$ ,  $\varepsilon_j = 3$  ( $1 \leq j \leq 3$ ),  $\tau = 2.147 10^{-1}$ ,  $\eta_{\max} = 10$ ,  $n = 16$  and  $\eta_\star = 5$ .

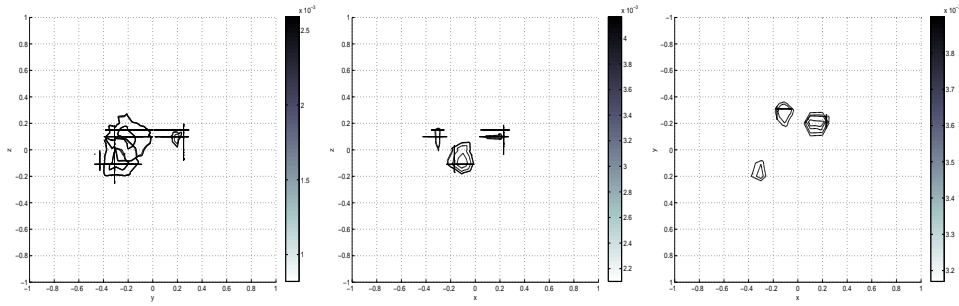


FIGURE 36. Contour-plot views respectively from the  $x$ -direction, the  $y$ -direction and the  $z$ -direction, based on the enriched sequence, deriving from one of the modules of the terms that approximate those of (27). Here,  $\mathcal{T}_h^4$  is used,  $\mu_j = 3$ ,  $\varepsilon_j = 10$  ( $1 \leq j \leq 3$ ),  $\tau = 2.147 10^{-1}$ ,  $\eta_{\max} = 10$ ,  $n = 16$  and  $\eta_\star = 5$ .

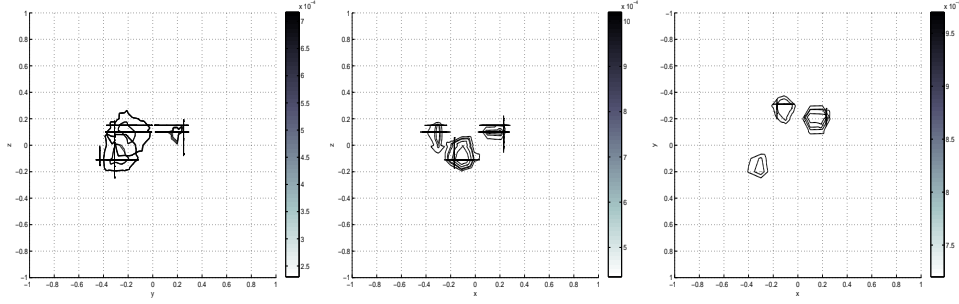


FIGURE 37. Contour-plot views respectively from the  $x$ -direction, the  $y$ -direction and the  $z$ -direction, based on the enriched sequence, deriving from one of the modules of the terms that approximate those of (27). Here,  $\mathcal{T}_h^4$  is used,  $\mu_j = 5$ ,  $\varepsilon_j = 3$  ( $1 \leq j \leq 3$ ),  $\tau = 2.147 \cdot 10^{-1}$ ,  $\eta_{\max} = 10$ ,  $n = 16$  and  $\eta_* = 5$ .

by considering the same number of measurements as in the previous multiple imperfections configuration, since we are dealing with the same region of interest in the procedure, as for  $\mathcal{T}_h^4$ .

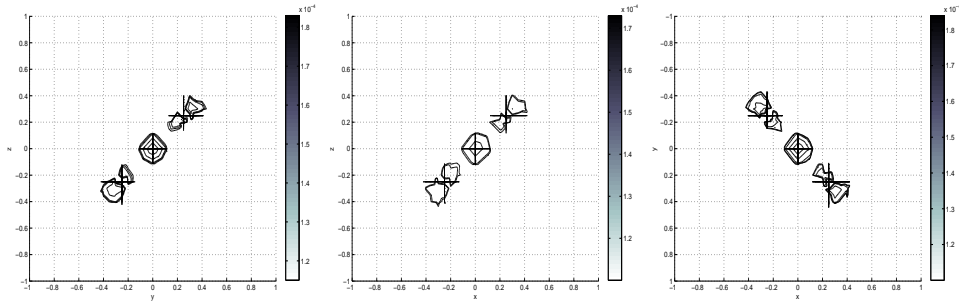


FIGURE 38. Contour-plot views respectively from the  $x$ -direction, the  $y$ -direction and the  $z$ -direction, based on the enriched sequence, deriving from one of the modules of the terms that approximate those of (27). Here,  $\mathcal{T}_h^5$  is used,  $\mu_j = 1$ ,  $\varepsilon_j = 3$  ( $1 \leq j \leq 5$ ),  $\tau = 2.26 \cdot 10^{-1}$ ,  $\eta_{\max} = 10$ ,  $n = 16$  and  $\eta_* = 4.5$ .

Figures 39 - 40 show the results of the localization in the electromagnetic case, also obtained from  $\mathcal{T}_h^5$ . Similar results come from simulations achieved with other physical contrasts ( $\mu_j = 5, 3$ ,  $\varepsilon_j = 10 + 0.1i$  for example), by using different frequencies and the same number of measurements as here.

As observed from simulations, the localization, both of a single imperfection and of multiple imperfections, is successfully achieved at frequencies that are not too low or too high. However, the present procedure appears, with the chosen value for  $\eta_{\max}$ , less efficient than the one based on the MUSIC approach, since the obtained results are less accurate and a larger number of measurements is required here. To improve the localization accuracy, large values for  $\eta_{\max}$  must be considered. However, for such values, the number of measurements to evaluate becomes very large and leads to a disadvantage of the procedure as regards the localization CPU time, despite the cutoff process of the Fourier domain.

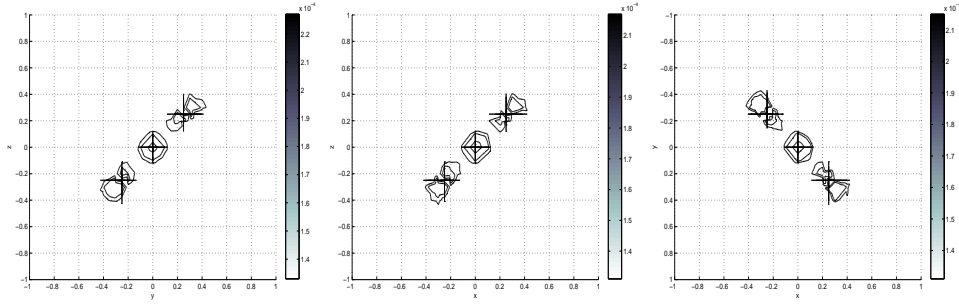


FIGURE 39. Contour-plot views respectively from the  $x$ -direction, the  $y$ -direction and the  $z$ -direction, based on the enriched sequence, deriving from one of the modules of the terms that approximate those of (27). Here,  $\mathcal{T}_h^5$  is used,  $\mu_j = 5$ ,  $\varepsilon_j = 3$  ( $1 \leq j \leq 5$ ),  $\tau = 2.26 \cdot 10^{-1}$ ,  $\eta_{\max} = 10$ ,  $n = 16$  and  $\eta_* = 4.5$ .

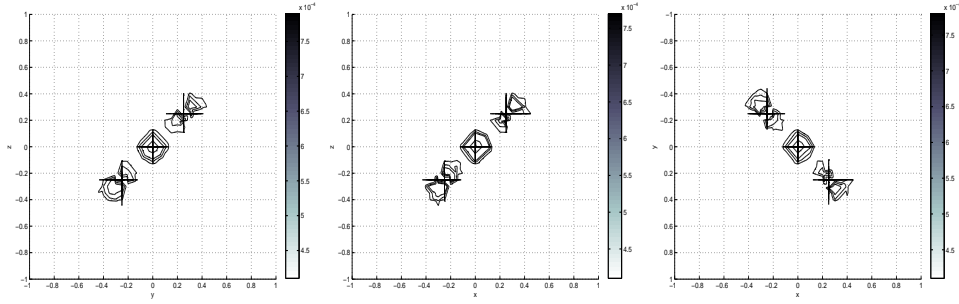


FIGURE 40. Contour-plot views respectively from the  $x$ -direction, the  $y$ -direction and the  $z$ -direction, based on the enriched sequence, deriving from one of the modules of the terms that approximate those of (27). Here,  $\mathcal{T}_h^5$  is used,  $\mu_j = 3$ ,  $\varepsilon_j = 10$  ( $1 \leq j \leq 5$ ),  $\tau = 2.26 \cdot 10^{-1}$ ,  $\eta_{\max} = 10$ ,  $n = 16$  and  $\eta_* = 4.5$ .

Since we can consider the same number of measurements to locate, at a fixed order of resolution, both the single imperfection as well as all the imperfections, in the same region of interest, we notice that the procedure appears more suitable for configurations with a large number of imperfections.

## 6. Conclusions and Perspectives

A framework for numerical simulations of the localization of small electromagnetic imperfections, in a three-dimensional bounded domain, has been described here. Based on the combination of an asymptotic formula for boundary measurements, a reduced mesh and a suited inversion algorithm, this framework has been validated in various contexts. Cases of a single imperfection and of multiple imperfections have been considered on the one hand, and three inversion algorithms have been used: the Current Projection method, the MUSIC algorithm, and an Inverse Fourier method. Independently of the inversion algorithms used, we conclude from simulations that it is not necessarily useful to consider a “very fine” reduced mesh in order to obtain a pertinent localization. Our numerical investigations have been done with respect to the parameter  $\tau$  (linking the frequency with the common order

of magnitude  $\alpha$  of the diameters of the imperfections), and not with respect to the wavelength for possibly describing a link with the distances between the imperfections, since the asymptotic formula for perturbations is developed with respect to  $\alpha$  and as on the other hand we take into account the numerical observations of [6] established by reconsidering with respect to  $\tau$  this formula for perturbations. Also in the multiple imperfections context, and now with very different orders of magnitude of the diameters, for instance when the setting associated with  $\mathcal{T}_h^4$  is modified in such a way that its last imperfection is now of one order of magnitude larger, we think that the reduced mesh for such a setting should be built as the one distinguished by  $\mathcal{T}_h^4$  but taking into account a conforming discretization of the imperfection whose diameter is one order of magnitude larger.

Comparisons performed in the case of a single imperfection (with the Current Projection method) or in the settings of multiple imperfections (with the MUSIC approach) show that the localization based on the Inverse Fourier method is numerically less efficient. This inversion method requires a larger number of measurements in order to provide an accurate localization and leads consequently to a very expensive CPU time — the evaluation of each measurement having a relatively important cost (average CPU time of about 27.7 s. on an “IBM Multi-Processor Power4 each one with a frequency of 1.1 GHz”, in the case of  $\mathcal{T}_h^5$  for example, without taking into account the CPU time for calculating the right-hand side of (16) associated with the measurement). Nevertheless this inversion method appears more suitable for configurations with a large number of imperfections, contrary to the MUSIC approach.

As opposed to a recent work developed in [6], and based on the use of full meshes, the present framework allows us: to achieve numerical simulations of the localization of imperfections of much smaller sizes, and to consider experiments in the configuration of a bigger number of imperfections.

A first perspective of the present work concerns the numerical localization of imperfections as small as here, from the same inversion procedures, but where the step of the numerical evaluation of boundary measurements will be achieved with the help of integral equation techniques.

Another perspective would be to study the numerical localization of such small imperfections from an approach using the same inversion procedures, but based on a variant of the multiscale finite element method ([13], [14]) for numerically evaluating boundary measurements. In fact, this approach could be helpful in the context of a large number of such imperfections in the domain.

## References

- [1] H. Ammari, E. Iakovleva & D. Lesselier, “A MUSIC algorithm for locating small inclusions buried in a half-space from the scattering amplitude at a fixed frequency”, *Multiscale Model. Simul.*, 3, (2005), 597–628.
- [2] H. Ammari, E. Iakovleva, D. Lesselier & G. Perrusson, “MUSIC-type electromagnetic imaging of a collection of small three-dimensional inclusions”, *SIAM J. Sci. Comput.*, 29, (2007), 674–709.
- [3] H. Ammari & H. Kang, *Reconstruction of small inhomogeneities from boundary measurements*, Lecture Notes in Mathematics, v. 1846, Springer-Verlag, Berlin, 2004.
- [4] H. Ammari, M. Vogelius & D. Volkov, “Asymptotic formulas for perturbations in the electromagnetic fields due to the presence of imperfections of small diameter II. The full Maxwell equations”, *J. Math. Pures Appl.*, 80, (2001), 769–814.
- [5] H. Ammari & D. Volkov, “Asymptotic formulas for perturbations in the eigenfrequencies of the full Maxwell equations due to the presence of imperfections of small diameter”, *Asymptot. Anal.*, 30, (2002), 331–350.

- [6] M. Asch & S.M. Mefire, “Numerical Localization of Electromagnetic Imperfections from a Perturbation Formula in Three Dimensions”, *Journal of Computational Mathematics*, 26, (2008), 149–195.
- [7] M. Brühl & M. Hanke, “Numerical implementation of two noniterative methods for locating inclusions by impedance tomography”, *Inverse Problems*, 16, (2000), 1029–1042.
- [8] A.P. Calderón, “On an inverse boundary value problem”, *Seminar on Numerical Analysis and its Applications to Continuum Physics, Soc. Brasileira de Matemática, Rio de Janeiro*, (1980), 65–73.
- [9] D.J. Cedio-Fengya, S. Moskow and M.S. Vogelius, “Identification of conductivity imperfections of small diameter by boundary measurements. Continuous dependence and computational reconstruction”, *Inverse Problems*, 14, (1998), 553–595.
- [10] D. Colton & R. Kress, *Integral equation methods in scattering theory*, Krieger Publ. Co., Malabar, Florida, 1992.
- [11] D.C. Dobson & F. Santosa, “An image-enhancement technique for electrical impedance tomography”, *Inverse Problems*, 10, (1994), 317–334.
- [12] G.B. Folland, *Introduction to partial differential equations*, Princeton University Press, Princeton, 1976.
- [13] T.Y. Hou, X.-H. Wu, “A multiscale finite element method for elliptic problems in composite materials and porous media”, *J. Comput. Phys.*, 134, (1997), 169–189.
- [14] T.Y. Hou, X.-H. Wu, Z. Cai, “Convergence of a multiscale finite element method for elliptic problems with rapidly oscillating coefficients”, *Math. of Comp.*, 68, (1999), 913–943.
- [15] R.V. Kohn & A. McKenny, “Numerical implementation of a variational method for electrical impedance tomography”, *Inverse Problems*, 6, (1990), 389–414.
- [16] J. Laminie & S.M. Mefire, “Three-dimensional computation of a magnetic field by mixed finite elements and boundary elements”, *Appl. Numer. Math.*, 35, (2000), 221–244.
- [17] T.D. Mast, A. Nachman & R.C. Waag, “Focusing and imaging using eigenfunctions of the scattering operator”, *J. Acoust. Soc. Am.*, 102, (1997), 715–725.
- [18] J.-C. Nédélec, “Mixed finite elements in  $\mathbb{R}^3$ ”, *Numer. Math.*, 35, (1980), 315–341.
- [19] J.-C. Nédélec & J. Planchard, “Une méthode variationnelle d’éléments finis pour la résolution numérique d’un problème extérieur dans  $\mathbb{R}^3$ ”, *Rev. R.A.I.R.O.*, 7, (1973), R-3, 105–129.
- [20] F. Santosa & M.S. Vogelius, “A backprojection algorithm for electrical impedance imaging”, *SIAM J. Appl. Math.*, 50, (1990), 216–243.
- [21] E. Somersalo, M. Cheney, D. Isaacson & E. Isaacson, “Layer-stripping: a direct numerical method for impedance imaging”, *Inverse Problems*, 7, (1991), 899–926.
- [22] D. Volkov, “Numerical methods for locating small dielectric inhomogeneities”, *Wave Motion*, 38, (2003), 189–206.

M. Asch, LAMFA, CNRS, Université de Picardie, 33, rue Saint-Leu, 80039 Amiens, France

S.M. Mefire, CMAP, CNRS, Ecole Polytechnique, Route de Saclay, 91128 Palaiseau, France.